Czech Technical University in Prague

Faculty of Nuclear Sciences and Physical Engineering

Department of Physical Electronics

DOCTORAL THESIS

Periodically poled nonlinear crystals for difference frequency generation of fiber lasers

Author: Ing. Yauhen Baravets
Supervisor: Dr. Ing. Pavel Honzátko
Advisor: Doc. Ing. Ivan Richter, Dr.
Date: 9.2020

Bibliographic Entry

Author	Ing. Yauhen Baravets CzechTechnical University in Prague Faculty of Nuclear Sciences and Physical Engineering Department of Physical Electronics
Title of Dissertation	Periodically poled nonlinear crystals for difference frequency generation of fiber lasers
Degree Programme	Application of Natural Sciences
Field of Study	Physical Engineering
Supervisor	Dr. Ing. Pavel Honzátko Institute of Photonics and Electronics of the CAS
Supervisor specialist	Doc. Ing. Ivan Richter, Dr. Czech Technical University in Prague Faculty of Nuclear Sciences and Physical Engineering Department of Physical Electronics
Academic Year	2019/2020
Number of Pages	86
Keywords	narrowband fiber laser, difference frequency generation, periodical poling, mid-infrared absorption spectroscopy

Acknowledgements

I would like to express my sincere gratitude to my supervisor, Pavel Honzátko, for giving me opportunity to work in the Institute of Photonics and Electronics of the Czech Academy of Sciences and for funding my work. I also wish to thank him for his patience and guidance during my study. Many thanks to co-supervisor Doc. Ivan Richter for the guidance and useful advice. Special thanks to my colleagues Prof. Jiří Čtyroký and Pavel Koška for their valuable comments and fruitful discussions. Thank to my colleagues Pavel Peterka, Filip Todorov, Ivo Bartoň and Doc. Petar Gladkov for their help and many practical advice. I would like to express my big gratitude to my family for their complete support.

This dissertation was funded from the projects MŠMT LD 14112/020041 Mid-Infrared Radiation Generation, Delivery and Applications and TAČR TA 02010825/082542 Widely tunable mid-infrared signal source for spectroscopy and metrology.

Declaration

I hereby declare that the presented work is my own and I have cited all sources I have used in the bibliography.

Prague, September 20, 2020 Yauhen Baravets

Abstract

Many gases have their fundamental vibration and rotational-vibrational absorption bands within a mid-infrared wavelength range and they can be detected by laser spectroscopy. But there is still a lack of widely tunable commercially available laser sources in a mid-infrared region.

This work is devoted to the development of narrow-band widely tunable mid-IR generator based on a difference frequency generation in periodically poled KTA and KTP crystals. The crystals are used to mix the beams from high-power fiber lasers working at 1060 nm and 1550 nm spectral bands. Several techniques for the fiber laser line narrowing are explored. The best result of 11.7 kHz is obtained for the fiber laser with a fiber ring resonator filter and active stabilization of the resonator length. The difference frequency generation process is numerically modeled using finite element method and the simulations results are in a good agreement with the experiment. Fabrication of the periodically poled nonlinear crystals at our facility is also described. With the mid-IR source based on the KTA crystal, we achieved tunability of 520 nm centered at 3.3 μm, which is twice as large as tunability of the source based on the KTP crystal. Finally, preliminary results of the spectroscopic experiments with a designed mid-IR laser are presented.

Abstrakt

Mnoho plynů má své základní vibrační a rotačně-vibrační absorpční čáry v rozsahu vlnových délek středního infračerveného pásma a lze je detekovat laserovou spektroskopií. Stále však existuje nedostatek široce laditelných komerčně dostupných laserových zdrojů ve střední infračervené oblasti.

Tato práce je věnována vývoji úzkopásmového široce laditelného generátoru pro střední infračervenou oblast založeného na generování rozdílového kmitočtu v periodicky pólovaných krystalech KTA a KTP. Krystaly se používají pro směšování signálů z vysoce výkonných vláknových laserů pracujících ve spektrálních pásmech kolem 1060 nm a 1550 nm. Je studováno několik metod pro zúžení čáry vláknových laserů. Nejlepší výsledek 11.7 kHz byl dosažen u vláknového laseru s vláknovým kruhovým rezonátorovým filtrem a aktivní stabilizací délky rezonátoru. Proces generování rozdílového kmitočtu je numericky modelován pomocí metody konečných prvků a výsledky simulací jsou v dobré shodě s experimentem. Také je popsána výroba periodicky pólovaných nelineárních krystalů připravených ve vlastním zařízení. Ve střední infračervené oblasti dosáhl zdroj založený na krystalu KTA přeladitelnosti 520 nm kolem 3,3 μm, co odpovídá dvounásobné přeladitelnosti zdroje založeného na krystalu KTP. Nakonec jsou prezentovány předběžné výsledky spektroskopických experimentů s navrženým laserem pro střední infračervenou oblast.

Contents

List of Figures

List of Tables

1 Introduction

Characterization of a variety of species in the gas phase is crucial in ecological, medical, scientific and industrial applications. For example, biomedical applications are of particular interest for diagnosis of diseases characterized by a distinctive breath-print that is based on the profile of numerous blood-borne volatile organic compounds [1], [2]; dynamic control of gaseous substances concentration is essential during numerous industrial processes [3]; and monitoring of leaks of chemical compounds or traces of dangerous chemical substances is very important in everyday life [4]. Laser absorption spectrometry is a suitable technique to measure the concentration or amount of many gases. The only disadvantage of the technique is that the absorption of the species is weak in visible and near-infrared ranges and the laser power is experiencing insignificantly changes during the light propagation through the sample. These changes are hardly detectable and limit the sensitivity of the technique. On the other hand, the fundamental rovibrational absorption bands of many molecules fall into the mid-infrared (MIR) spectral range [5]. These lines are more intense than their overtones in the visible and near-infrared spectral ranges. This fact, together with the presence of several mid-IR atmospheric windows with high transmission, permits more sensitive spectroscopic measurements. For the purpose of high-resolution molecular spectroscopy tunable narrowband continuous-wave (CW) mid-infrared laser sources are an ideal solution. Sensitivity can be also improved by using a longer path length of the transmitted laser beam in a sample. Special external cavities filled with the tested species are ordinarily used. Highly-reflected mirrors of the cavity form the multi-pass cells, i.e. Fabry-Perot resonators, or White or Herriott cells, where the interaction length is increased from $\sim$2 to $\sim$5 orders of magnitude. Additionally, employing appropriate optical signal detection techniques helps to improve the sensitivity and increase the signal-to-noise ratio. Modulated techniques (wavelength or frequency), as well as a variety of cavity-enhanced techniques, have detection sensitivities ranging from parts per million by volume (ppmv) to parts per trillion by volume (pptv) levels depending on the specific gas species and described in detail in [6, 7],[C8].

To obtain the high-resolution measurement the laser linewidth should be significantly smaller than the absorption line of the molecule. The width of absorption line is affected by Doppler broadening and collisional broadening. Usually, the pressure of the sample is decreased to the value where Doppler and collisional broadening is equal. In this case, the absorption linewidth of the most molecules is a few hundreds of MHz, and the high-resolution measurement can be done with the laser linewidth of $\sim$ 1MHz or lower and tunability of at least several hundreds of MHz. Such narrow linewidth is inherent to CW lasers, or even narrower to single longitudinal mode CW lasers, and hard to reach in pulsed lasers. Decreased pressure, when the lines are narrow, also allows to achieve good selectivity in gas mixtures [8]. We can summarize, that for the successful high-resolution spectroscopy experiment the tunable CW mid-IR laser source with the linewidth up to 1 MHz is needed, and the output power of the laser should be at the level of 0.1–1 mW to provide sufficient signal-to-noise

ratio.

Over the last ten years, the group of MIR laser sources suitable for laser spectroscopy has mainly included a few sorts of devices. Transition metal doped II-VI chalcogenide lasers, especially $Cr^{2+} : ZnSe$ and $Cr^{2+} : ZnS$, have a wide tunability, Watt-level CW output power, narrow linewidth $\sim$ 100 kHz. However, all of this is true only for the spectral region below 3 μm, for the wavelengths longer than 3 μm a significantly lower gain, thermal lens effect, complex optical pump with Tm-doped fiber lasers, relatively wide linewidth ($\sim$ 20 MHz) for CW operation [9], limit the usefulness of $Cr^{2+} : ZnSe$ and $Cr^{2+} : ZnS$ lasers for the spectroscopy in this region. Er-, Ho-, and Dy-doped fluoride fibers can be used as an active medium for lasing beyond 3 μm [10,11]. Wide tunability for fluoride fiber lasers working in CW regime has been recently published in [12,13], but the linewidths of these lasers are relatively wide ($\sim$GHz). Additionally, not mature fabrication technology of fluoride fiber components, complex dual-lasers optical pump, and non-all-fiber structure do not allow these lasers to have extensive use in high-resolution molecular spectroscopy. Well-known lead-salt diode lasers meet all requirements and are broadly used for absorption spectroscopy [14]. The main disadvantages are operation at temperatures below 200 K and narrow wavelength tuning, only a few nanometers. Another diode lasers, quantum cascade lasers (QCLs) and very similar interband cascade lasers (ICLs), are able to work at room temperature and actively used as mid-infrared spectroscopic sources for many years [7, 15, 16]. While ICLs are employed mainly in 3–5 μm spectral band, QCLs demonstrate the best performance in a much wider range from 3 to 12 μm [17]. Despite the possibility of operating in CW regime at room temperature [18,19], distributed feedback (DFB) QCLs and ICLs, which provide single-frequency operation, can be tuned only in a narrow range $\sim$ 10 nm. Using an external cavity, tunability of QCLs can be significantly improved and reaches up to 15% of the center wavelength with the linewidth of several MHz. Nowadays, QCLs look very perspective for the laser absorption spectroscopy in MIR, even though their price is high and the beam quality is not ideal. Of cause, there are several other promising sources for the high-resolution spectrometry in mid-IR, like supercontinuum sources [20] or frequency combs [21], but these sources are mainly based on pulsed lasers, which are out of the scope of the thesis.

Another types of mid-infrared lasers, where the radiation in 3–8 μm spectral band can be obtained by nonlinear frequency down-conversion generation, are optical parametric oscillators (OPO) and difference frequency generators (DFG) [22–26]. The mid-IR sources based on parametric nonlinear optical processes are portable and compact, have a good beam quality, do not need cryogenic cooling, demonstrate a small linewidth together with the widest tunability. In OPO a pump beam with the highest frequency produces in nonlinear medium two other beams, signal and idler, with lower frequencies. The nonlinear medium placed in a resonant cavity for the signal beam can significantly improve the efficiency of this parametric oscillation process. If the pump power is sufficiently high to exceed the resonator losses for the parametric gain at the signal wavelength, parametric oscillation will start. To conserve the energy, the mid-infrared idler

beam will be generated together with the signal. The efficiency of broadband continuously tunable CW OPO can be more than 75% [27] and the tunability can cover the spectral range from 3 to 16 μm, depending on the nonlinear medium. On the other hand, OPO resonator requires mirrors with a broadband dielectric coating, advanced tuning and frequency stabilization techniques to overcome the mode hopping.

Unlike in OPO, in the DFG process mixing of two input beams, pump and signal, produces the idler beam at the difference frequency of these beams. Despite the low efficiency, the main advantages of MIR sources based on the DFG are the possibility of using well-developed commercially available CW broadly tunable Yb- and Er-doped fiber lasers. These lasers have diffraction-limited beams and can operate in single longitudinal mode. Possibility to use fiber wavelength division multiplexers (WDM) simplifies the DFG alignment. Nowadays, both DFG and OPO based on periodically poled crystals and pumped by fiber lasers can achieve wide tunability in the mid-IR spectral range [C8]. In this thesis, we report on the design and performance of the broadly tunable narrowband CW mid-infrared DFG sources based on home-made fiber lasers. Also, we describe the process of fabrication of periodical domain patterns in potassium titanyl phosphate (KTP) and potassium titanyl arsenate (KTA) nonlinear crystals. The potential application of these sources is also presented.

2 Goals of the thesis

This work was mainly motivated by possibility of the creation of coherent mid-infrared radiation sources for panoramic high-resolution spectroscopy. Specifically, the goal of the thesis is a research of mid-infrared laser sources based on a difference frequency generation in nonlinear KTP and KTA crystals, delivery and exploitation of this radiation for the laser spectroscopy of gases. The particular aims of the dissertation are schematically depicted in the diagram (see Fig.1) and described below.

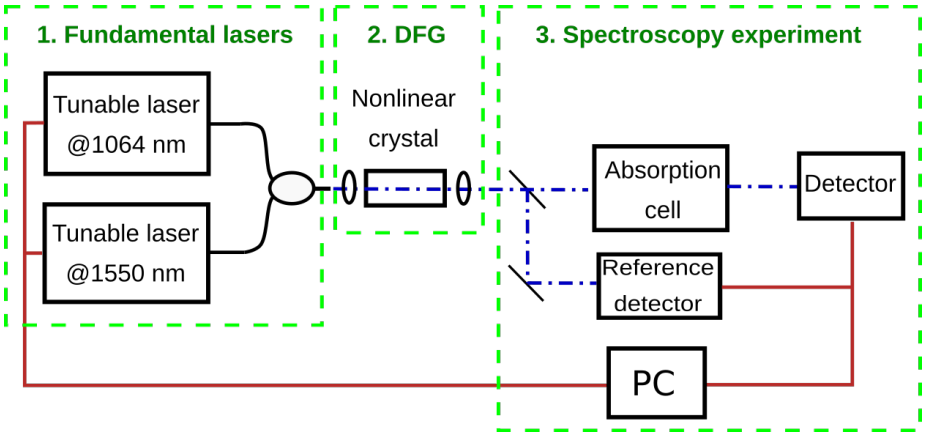

Figure 1: Problems covered in this thesis .

1. Development of CW narrowband tunable fiber lasers, pump and signal, at the central fundamental wavelengths of 1064 nm and 1550 nm. Research and optimization of lasers design for achieving narrow line and broad tunability. The desired laser linewidths are of the order of MHz or less and the tuning ranges are greater or equal to 50 nm.

2. Using the difference frequency generation process in periodically poled KTP and KTA crystals to obtain the mid-infrared radiation tunable near the wavelength of 3.3 μm. Comparison of the efficiency and tunability of two mid-IR devices based on these nonlinear crystals. Improvement and redesign of available technology of periodic poling of the crystals at ÚFE.

3. Demonstration of the usefulness of the developed mid-IR laser sources for the high-resolution panoramic absorption spectroscopy of gases.

3 Methods

3.1 Fiber lasers

The main advantages of fiber lasers are excellent heat management, beam quality $M^2 \approx 1$, simple alignment, availability of high average power operation, variety of wavelengths by doping with rare-earth elements. The main disadvantage is a material limitation for direct operation at ultraviolet (UV) range and MIR wavelengths longer than 13 μm. Moreover, the production technology is mature mainly for silica fibers, which are transparent even in shorter wavelength range up to 2.2 μm. But wide commercial availability of fiber components and Yb-, Er-, Tm- and Ho-doped active silica fibers allows to fabricate robust and high-power laser systems [28, 29], [C3,C4].

As it was mentioned in the second section 2, this work is mainly dedicated to the mid-infrared tunable DFG sources based on PPKTP and PPKTA crystals and further use such devices for the high-resolution laser absorption spectroscopy of gases. In our experiments we use CW fiber lasers to shift the working wavelength to the mid-IR region employing a nonlinear parametric effect. We have to note, that only Yb- and Er-doped fiber lasers are suitable as fundamental sources to obtain a mid-IR wavelength range near 3.3 μm by the DFG process. Additionally, broad tunability (∼100 nm) of Yb- and Er-doped fiber lasers near their central wavelengths of 1030 nm and 1550 nm, respectively, allows to obtain broad tunability of 3–3.8 μm in mid-IR. Other combinations of Yb-, Er-, Tm- and Ho-doped fiber lasers give the difference frequency near the wavelength bands near 2 μm, or longer than 5.9 μm. Generally, the 2-μm wavelength region can be directly reached by Ho-doped fiber lasers, and the wavelength region longer than 5.9 μm is out of our interest because of the low transmittance of KTP and KTA crystals (see Fig.3a).

The part of the thesis describing the fundamental fiber lasers around 1060 and 1550 nm wavelength regions is rather experimental and explained in detail in the section Experimental results4.

3.2 Difference frequency generation model

The basics of nonlinear optical interactions can be found, for example, in the very famous textbook [30]. For the difference frequency generation, in particular, more detailed information is provided in another textbook [31]. In this chapter, only the brief theory of DFG is provided for the consistency of the thesis. For those who are not familiar with the second-order nonlinear interactions and phase matching technique, we recommend referring to the literature mentioned above.

3.2.1 The coupled-wave equations for difference frequency generation

Suppose we have a nonlinear medium, so that the electric displacement is

$$\boldsymbol{\mathcal{D}} = \epsilon_0 \boldsymbol{\mathcal{E}} + \boldsymbol{\mathcal{P}}. \tag{1}$$

where $\boldsymbol{\mathcal{P}}$ is the induced polarization vector which can be expressed as a function of an applied electric field $\boldsymbol{\mathcal{E}}$:

$$\boldsymbol{\mathcal{P}} = \epsilon_0 \chi^{(1)} \boldsymbol{\mathcal{E}} + \epsilon_0 \left(\chi^{(2)} \boldsymbol{\mathcal{E}}^2 + \chi^{(3)} \boldsymbol{\mathcal{E}}^3 + ... \right), \tag{2}$$

where $\epsilon_0$is the permittivity of vacuum and $\chi^{(m)}$ is the susceptibility tensor of m-th order. This work mainly concerns the DFG process in non-centrosymmetric crystals which is based on the second-order nonlinearity $\chi^{(2)}$. In literature susceptibility tensor $\chi^{(2)}$ is often changed by a tensor of nonlinear coefficients $d = \frac{1}{2}\chi^{(2)}$. After applying Kleinman symmetry [30] this d-tensor can be written in a form of a 3×6-element matrix:

$$d = \begin{bmatrix} d_{11} & d_{12} & d_{13} & d_{14} & d_{15} & d_{16} \\ d_{21} & d_{22} & d_{23} & d_{24} & d_{25} & d_{26} \\ d_{31} & d_{32} & d_{33} & d_{34} & d_{35} & d_{36} \end{bmatrix}. \tag{3}$$

The medium is nonmagnetic and magnetic induction is

$$\boldsymbol{\mathcal{B}} = \mu_0 \boldsymbol{\mathcal{H}}, \tag{4}$$

where μ_0 is the permeability of free space and $\boldsymbol{\mathcal{H}}$ is the magnetic intensity; with no currents ($\boldsymbol{\mathcal{J}} = 0$) and no free charges ($\rho = 0$). Maxwell's equations describe not only the generation of new components of the input field, but also how the various frequency components of the field are coupled by the nonlinear interaction:

$$\begin{aligned} \nabla \times \boldsymbol{\mathcal{E}} + \frac{\partial \boldsymbol{\mathcal{B}}}{\partial t} = 0, \qquad & \nabla \cdot \boldsymbol{\mathcal{D}} = 0, \\ \nabla \times \boldsymbol{\mathcal{H}} - \frac{\partial \boldsymbol{\mathcal{D}}}{\partial t} = 0, \qquad & \nabla \cdot \boldsymbol{\mathcal{B}} = 0. \end{aligned} \tag{5}$$

Taking the curl of the first equation in this system $\nabla \times \nabla \times \boldsymbol{\mathcal{E}} + \frac{\partial}{\partial t}\mu_0 \left(\nabla \times \boldsymbol{\mathcal{H}} \right) = 0$, and using the third equation in the system and eq. (1) to replace $\nabla \times \boldsymbol{\mathcal{H}}$ by $\epsilon_0 \frac{\partial \boldsymbol{\mathcal{E}}}{\partial t} + \frac{\partial \boldsymbol{\mathcal{P}}}{\partial t}$ and $\mu_0$by $\frac{1}{\epsilon_0 c^2}$ we obtain

$$\nabla \times \nabla \times \boldsymbol{\mathcal{E}} + \frac{1}{c^2} \frac{\partial^2 \boldsymbol{\mathcal{E}}}{\partial t^2} = -\frac{1}{\epsilon_0 c^2} \frac{\partial^2 \boldsymbol{\mathcal{P}}}{\partial t^2}. \tag{6}$$

The left side of eq.(6) can be written in form $\nabla \times \nabla \times \boldsymbol{\mathcal{E}} = \nabla \cdot (\nabla \cdot \boldsymbol{\mathcal{E}}) - \nabla^2 \boldsymbol{\mathcal{E}}$. In nonlinear optics the contribution of $\nabla \cdot (\nabla \cdot \boldsymbol{\mathcal{E}})$ is negligible, since divergence $\nabla \cdot \boldsymbol{\mathcal{E}} = 0$ even in birefringent media, and can usually be dropped for simplicity. Splitting the material polarization $\boldsymbol{\mathcal{P}}$ into linear and nonlinear parts as $\boldsymbol{\mathcal{P}} = \boldsymbol{\mathcal{P}}^{(1)} + \boldsymbol{\mathcal{P}}^{NL}$, we can write:

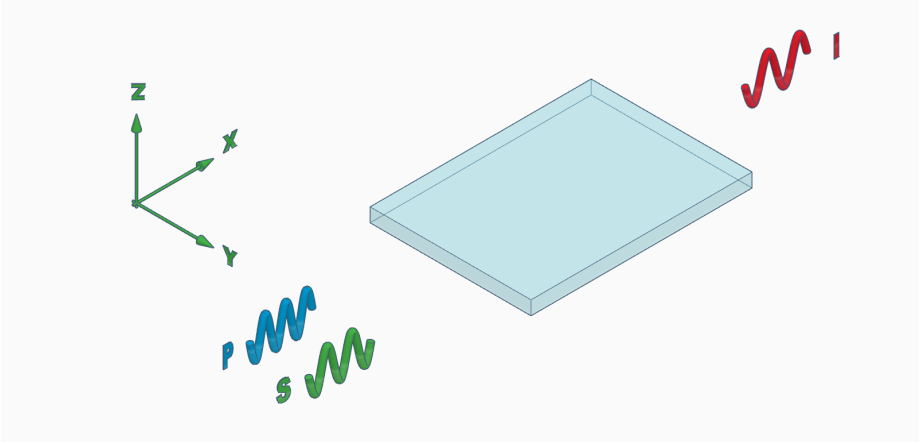

Figure 2: Light propagation inside the crystal

$$\nabla^2 \boldsymbol{\mathcal{E}} - \mu_0 \frac{\partial^2 \left(\epsilon_0 \boldsymbol{\mathcal{E}} + \boldsymbol{\mathcal{P}}^{(1)}\right)}{\partial t^2} = \frac{1}{\epsilon_0 c^2} \frac{\partial^2 \boldsymbol{\mathcal{P}}^{NL}}{\partial t^2}. \tag{7}$$

Introducing relative permitivity as $\epsilon_r = 1 + \chi^{(1)} = n^2$, where n is a refractive index of the medium, we can finally obtain the wave equation [30]:

$$\nabla^2 \boldsymbol{\mathcal{E}} - \frac{\epsilon_r}{c^2} \frac{\partial^2 \boldsymbol{\mathcal{E}}}{\partial t^2} = \frac{1}{\epsilon_0 c^2} \frac{\partial^2 \boldsymbol{\mathcal{P}}^{NL}}{\partial t^2}. \tag{8}$$

Throughout this thesis x (crystalline a-axis) is chosen as the propagation axis (see Fig.2). Using the complex amplitudes we can express electric field and polarization for all beams propagating along x axis as

$$\begin{aligned} \boldsymbol{\mathcal{E}}_q &= \frac{1}{2} \left\{ \boldsymbol{E}_q \exp\left[i\left(\omega_q t - k_q x\right)\right] + c.c. \right\} \\ \boldsymbol{\mathcal{P}}_q &= \frac{1}{2} \left\{ \boldsymbol{P}_q \exp\left[i\left(\omega_q t - k_q x\right)\right] + c.c. \right\} \end{aligned}, \tag{9}$$

where $k_q = \frac{n_q \omega_q}{c}$ is a wave number of the q-beam (q=p, s, i, are pump, signal and idler beams). Now we can rewrite the term $\nabla^2 = \frac{\partial^2}{\partial x^2} + \nabla_\perp^2$ and take the second time derivatives from the electric field and polarization. Using the approximation of slowly varying electric field amplitude along the direction of propagation $\left(\frac{\partial^2 \boldsymbol{\mathcal{E}}}{\partial x^2} \ll k \frac{\partial \boldsymbol{\mathcal{E}}}{\partial x}\right)$, and the fact that for DFG process an angular frequency $\omega_i = \omega_p - \omega_s$ obey photon energy conservation, a simplified coupled wave equation for the idler field amplitude can be derived:

$$\frac{\partial \boldsymbol{E_i}}{\partial x} + \frac{i}{2k_i} \nabla_\perp^2 \boldsymbol{E_i} = -i \frac{d_{eff} \omega_i}{2 n_i c} \boldsymbol{E_p} \boldsymbol{E_s^*} \exp\left(-i \triangle k x\right). \tag{10}$$

In this equation d_{eff} is an effective nonlinear coefficient and $\triangle k = k_p - k_s - k_i$ is a wave vector mismatch due to material dispersion. Here we should mention, that two other equations for pump and signal waves were omitted because of very low efficiency of DFG process and assumption of no pump and signal depletion, as a result, the nonlinear conversion does not affect the amplitude of fundamental waves significantly. To solve this equation we will make a few assumptions.

Firstly, we assume that the focusing system does not have significant aberrations, especially astigmatism, and cylindrical symmetry can be employed. Rewriting the Laplacian in cylindrical coordinates leads to the equation form

$$\frac{\partial \boldsymbol{E_i}}{\partial x} + \frac{i}{2k_i\rho}\frac{\partial \boldsymbol{E_i}}{\partial \rho} + \frac{i}{2k_i}\frac{\partial^2 \boldsymbol{E_i}}{\partial \rho^2} = -i\frac{d_{eff}\omega_i}{2n_i c}\boldsymbol{E_p}\boldsymbol{E_s^*}\exp\left(-i\triangle k x\right), \qquad (11)$$

where ρ – is a radius of cylindrical region inside the crystal. In our case, maximum ρ is the half of the crystal thickness h and equal to 0.5 mm.

Secondly, we assume that the beams are not strongly diverging and the paraxial approximation can be used. Now the intensity distribution of the idler beam can be expressed as a magnitude of the time averaged Poynting vector

$$I_i(x,y,z) = \frac{|Re(\boldsymbol{\mathcal{E}} \times \boldsymbol{\mathcal{H}}^*)|}{2} = \frac{n_i|\boldsymbol{E}_i(x,y,z)|^2}{2\eta}\ , \qquad (12)$$

where η is the wave impedance of the medium (for free space, $\eta \approx 377\Omega$). As the intensity of the beam is the power transferred per unit area, the full power of the generated idler beam in cylindrical coordinates is

$$P_i = \int_0^{h/2}\int_0^{2\pi} I_i \rho \partial\rho\partial\varphi = 2\pi\int_0^{h/2}\rho I_i \partial\rho, \qquad (13)$$

here I_i is the intensity (12) in a cross-section of interest. The output power P_i is an integral over the output face of the crystal.

Equation 10 can be solved analytically for the plane waves interaction [30,31], but for the real systems with non-plane waves the solution can be found only with some assumptions and simplifications. We will discuss some of them later in section 3.4.

3.2.2 Phasematching and nonlinear coefficient

The efficiency of DFG is maximized when the phase-mismatch between the pump, signal and idler beams is $\triangle k = 0$, but it is achievable only for certain wavelengths and certain propagation directions inside the nonlinear medium because of the material dispersion. The phase-matching condition $\triangle k = 0$ in nonlinear materials can be reached in two ways: birefringent phase-matching (BPM) or quasi-phase-matching (QPM). The BPM method has some drawbacks: limited choice of appropriate crystals, inconvenient working angles and temperatures, Poynting vector walk-off. On the other hand, the QPM method is suitable for any wavelength within the transparency region of the material and

it can work with the use of the largest element of the tensor of nonlinear susceptibility. QPM, as it is well known [32], requires a micrometer-scale periodic structure inside the material with the alternately changing sign of the nonlinear coefficient $+d$ and $-d$. This periodical reversal nonlinear domains pattern inside the crystal has a wave vector of $K = \frac{2\pi}{\Lambda}$, where Λ is a period of the QPM grating. The most favorite materials for the QPM are ferroelectrics like lithium niobate, potassium titanyl phosphate, etc. In order to exploit the highest nonlinear coefficient of these crystals d_{33}, all three interacting waves should propagate along x-axis and be linearly polarized along z-axis. It is very convenient because we can launch the pump and the signal beams collinearly along the crystal axes to avoid Poynting vector walk-off and thus increase the length of nonlinear interaction to produce the idler beam. But in this case because of the different phase velocities of the interacting waves the phase mismatch $\triangle k = k_p - k_s - k_i$ is not equal to 0 and additional parameter K of the periodical structure inside the crystal helps to compensate the phase mismatch between the propagating waves. The process of implementing the periodic structure inside nonlinear crystals will be described later in the experimental part 4.5.

3.3 Crystal selection

In general, the most frequently used nonlinear crystal for the QPM DFG is lithium niobate (LiNbO3, LN). At the very beginning, bulk periodically poled congruent LN were employed. They performed well, but it was difficult to modulate the sign of nonlinear coefficient [33]. In turn, MgO doping (ordinary 5%) and stoichiometric composition of lithium niobate helped significantly improve the laser damage resistance and decrease a coercive field under 5 kV/mm preserving a high nonlinear coefficient. All this together with the mature growing and periodically poling technology, and wide tunability makes lithium niobate a good candidate for the mid-IR generators. In this work, the developed fiber lasers at the DFG fundamental wavelengths ($\sim$1060 nm and $\sim$1550 nm) are able to generate $>$1 W of power and for the beam waist size $\sim$ 30 μm inside the crystal the intensity reaches $\sim$ 350 MW/cm^2. Such high power densities are undesirable even to stoichiometric LN. On the other hand, even higher intensities are still rather safe for potassium titanyl phosphate ($KTiOPO_4$ or KTP) and its isomorph potassium titanyl arsenate ($KTiOAsO_4$, KTA). Below in a Table 1 we will try to compare some properties of these three crystals which are the key properties to the effective DFG process and developed spectroscopic device. As can be seen, for KTP and its isomorphs the laser damage threshold at the pump wavelength is higher than 500 MW/cm^2, what is several times greater than for LN. Also, the higher refractive index of LN can cause higher losses for uncoated samples. The next important parameter is the nonlinear coefficient d_{33}. As will be shown later in Eq. 14, the idler power in mid-IR is proportional to the square of the nonlinear coefficient and the highest nonlinear coefficient is almost two times higher for LN than for KTP. Additionally, the crystal should be transparent in the working region. According to data from [41] KTA and LN crystals are transparent up to 5–5.5 μm (see Fig.3), while the transmission of

Crystal	Damage threshold @1064 nm [MW/cm^2]	Highest nonlinear coefficient @1064 nm d_{33} [pm/V]	Calculated tunability [nm]	Price [€/mm^3] [34]
KTP	>500 [35]	13.7 [36]	490	1.4
KTA	>500 [37]	16.2 [38]	895	4
MgO:SLN	>100 [39]	25 [40]	830	28

Table 1: Comparison of the properties of KTP, KTA, LN.

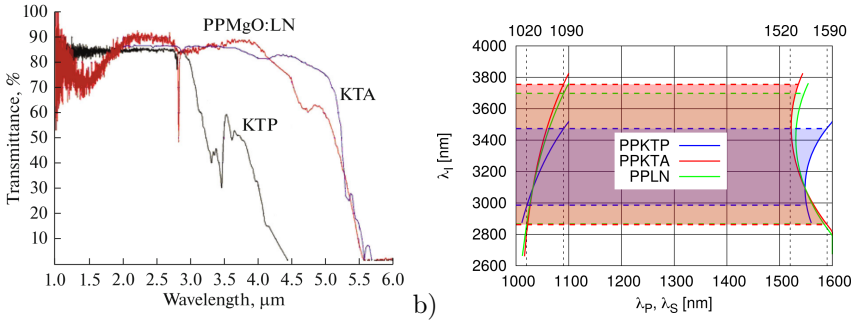

Figure 3: (a) Transmittance of KTP, KTA, and MgO:LN crystals [41]. (b) Tunability ranges for PPKTP and PPKTA compared with PPLN.

KTP drops significantly for λ>4 μm, but all of these three crystals can be used to generate the difference frequency of the developed tunable lasers near 3.3 μm. In Fig.3(b) there are maximal theoretical tunability ranges in the MIR region for the crystals calculated using the QPM condition for plane wave interaction $k_p - k_s - k_i - K = 0$ and working ranges of the pump and signal lasers of 1020–1090 nm and 1520–1590 nm respectively (marked with vertical dashed lines). According to these calculations, the maximum achievable tunability range for PPKTP (Sellmeier equation is taken from [25]) with the optimal poling period of 35.9 μm is 490 nm, for PPKTA (Sellmeier equation is from [26]) with the period of 39.8 μm is 895 nm, and PPLN (Sellmeier equation is from [42]) with the period of 30.4 μm has 830 nm. As we can see, PPKTA and PPLN can provide almost two times broader tunability than PPKTP. The last but not least parameter is the unit cost of the crystals. The flux grown KTP crystals have a price of 1.4 € for mm^3 and KTP crystals with better gray track resistance (GTRKTP) cost almost three times higher, what is comparable to KTA price. But the unit price for the stoichiometric MgO doped lithium niobate is roughly 20 times higher than for KTP, and this is one of the main reason for our choice of the KTP and KTA crystals for further poling experiments. In our lab we have available the basic equipment for fabrication of micrometer-scale periodic structure inside the KTP crystals and its isomorphs with dimensions (length

x width x thickness): 16.5×12×1 mm. One of the tasks of this thesis is to recommence this equipment and to possibly enhance the poling process of the crystals. We investigated the poling process on 6 KTP and 1 KTA crystals from CRYSTECH Inc. Five flux-grown KTP crystals were used for the initial experiments and optimization of the poling procedure, while one GTRKTP and one KTA were used for the final periodic poling process.

3.4 Optimization of the DFG process

The results of numerical modeling described here were firstly presented in a particular way in [C10,C11,C9,C5,C7] and published in [P1,C8].

Ordinary, the output power of any nonlinear process is relatively low and efficiency enhancement is one of the main tasks in the field. In this thesis focusing conditions of the fundamental beams and the wave vector mismatch $\triangle k$ are considered as the main possibilities to optimize the efficiency of the nonlinear DFG process. The focusing conditions can be easily changed by utilizing various lenses while the wave vector mismatch can be minimized by the periodical reversal of nonlinear domains pattern inside the crystal with the wave vector K ($\triangle k = k_p - k_s - k_i - K$).

To describe the nonlinear process in a more realistic system instead of the plane waves we will use the Gaussian beams. Boyd and Kleinman [43] obtained an analytical solution on nonlinear parametric interaction for focused Gaussian beams depending on the focusing factor. They found that for parametric nonlinear processes the optimal focusing conditions for non-critical phasematching are reached for the focusing parameter $\xi = \frac{l}{b} = \frac{l}{2z_R}$ of 2.84, where $b = 2z_R = \frac{2\pi n\omega_0^2}{\lambda}$ is a confocal parameter of a beam with a waist size ω_0, which is twice the Rayleigh length z_R. Later, this theory was studied in details by Chu and Broyer [44, 45]. Nowadays their theory is widely used for the calculation of the efficiency of the nonlinear optical processes [46–48]. Generalizing this theory for DFG process power of the idler beam can be written as

$$P_i = P_p P_s \frac{32\pi^2 d_{\text{eff}}^2 l}{\epsilon_0 c n_i \lambda_i^2 \left(n_s\lambda_p + n_p\lambda_s\right)} h\left(\xi, \sigma, \mu, \alpha, l\right) \tag{14}$$

where d_{eff} is the effective non-linear coefficient, l is the crystal length. The focusing function h is defined as:

$$h\left(\xi, \sigma, \mu, \alpha, l\right) = \frac{e^{\frac{-\alpha l}{2}}}{4\xi} \int_{-\xi}^{\xi} d\tau \int_{-\xi}^{\xi} d\tau' e^{-i\sigma\left(\tau-\tau'\right)+\frac{\alpha l}{4\xi}\left(\tau+\tau'\right)} \cdot \frac{1}{1+\tau\tau' - i\frac{1+\mu^2}{1-\mu^2}\left(\tau-\tau'\right)} \tag{15}$$

where

$$\xi = \frac{l}{b},\ \mu = \frac{n_s\lambda_p}{n_p\lambda_s},\ \sigma = -\pi b\left(\frac{n_p}{\lambda_p} - \frac{n_s}{\lambda_s} - \frac{n_i}{\lambda_i} - \frac{1}{\Lambda}\right) \tag{16}$$

α is the absorption coefficient. In this theory was assumed that all three interacting beams are Gaussian, focused in the middle of the crystal, and had equal confocal parameters $b_P = b_S = b_I$.

Finding the maximum of the focusing function h allows us to optimize the focusing conditions. For instance, Figure 4(a) shows the dependence of calculated output power in PPKTA crystal on the period of the QPM grating in KTA for various focal lengths of the focusing optics. The highest output power can be obtained for the focal length f of 33 mm (in practice we can use achromatic doublet AC254-030-C from Thorlabs with f=30 mm). For this value, the optimal focusing condition ξ is equal to 2.93 that is quite close to a value of 2.84 predicted by Boyd and Kleinman [43]. In general, the optimal focusing condition is a sort of trade-off between the tight focusing to obtain a high intensity beam waist ω_0 and interaction length l.

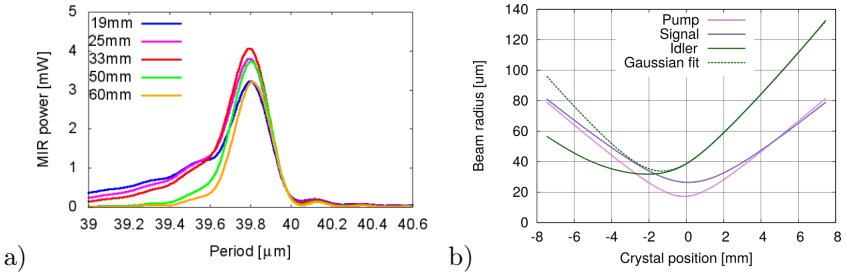

a) b)

Figure 4: (a) The dependence of DFG power in MIR on the period of the QPM grating in KTA for various focal lengths of the focusing optics. (b) FEM simulation of pump, signal and idler beams propagations in KTA crystal for the lens with f=30 mm.

In systems with one focusing lens, the pump and signal beams do not have the same confocal parameters and waist positions (see Fig.4(b)). Under such conditions, the wave equation (10) should be solved numerically. In this work, we explored the possibility to enhance the efficiency of DFG process. The numerical solution of the wave equation for the Gaussian beams allowed us to find the optimal focusing conditions. For this purpose, a multi-paradigm numerical computing environment MATLAB was used. Specifically, finite element method (FEM) was utilized to solve this initial-boundary value problem for parabolic partial differential equation. The author developed 2D code based on built-in function *solvepde* [49] for simulating the CW difference frequency generation by mixing three photons and using Gaussian laser beams.

Firstly, the output power of the DFG process was calculated for various poling periods in PPKTP and PPKTA. In this case, it was supposed that the beams are focused in the middle of the crystal and the optimal focusing condition obtained earlier from eq.(14) was used. The pump and signal powers are supposed to be equal $P_P = P_S = 1W$. Optimal poling periods for PPKTP and PPKTA crystals (see Fig.5) slightly differ from that, calculated for the plane waves interaction. It is interesting, that the calculated power of the idler beam

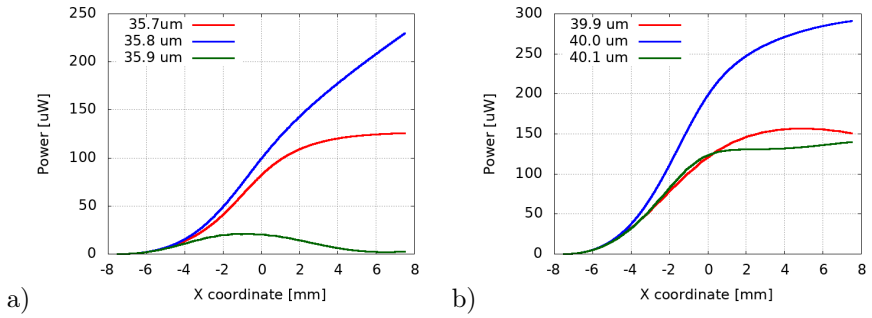

a) b)

Figure 5: DFG output power dependence on domain period for PPKTP (a) and PPKTA (b) for pump 1060 nm and signal 1550 nm fundamental wavelengths.

is more than 10 times lower than for the analytical solution 14 and, as we will see from an experiment, closer to the really measured power.

The next step was to investigate the impact of waist sizes ω_{0P}, ω_{0S} and their shifts relative to the middle of the crystal. The highest DFG power was obtained only when the pump and signal beams focused right to the middle of the nonlinear medium. The dependence of the idler beam power on various pump ω_{0P} and signal ω_{0S} waist sizes looks more interesting. In Figure6 such dependence for PPKTP crystal with the period of 35.9 μm is presented.

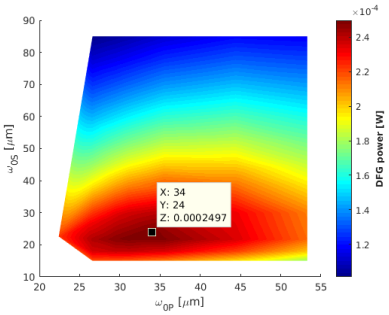

Figure 6: Calculated DFG idler power for PPKTP crystal with period of 35.9 μm for various pump ω_{0P} and signal ω_{0S} beam sizes.

As we see, the highest output power is achieved for $\omega_{0P} = 34\,\mu m$ and $\omega_{0S} = 24\,\mu m$, which corresponds for pump beam focusing parameter with $\xi_p \approx 2$ and tighter focusing parameter of signal beam with $\xi_s \approx 5$. In this situation, DFG efficiency enhancement by $\sim 5\%$, in comparison with the equal confocal parameter case $b_p = b_s$ ($\omega_{0P} = 22\,\mu m$ and $\omega_{0S} = 27\,\mu m$), can be reached. It is in consistence with the results published earlier in [50, 51], where the maximum output power of the optical parametric oscillation processes is achievable for unequal confocal parameters $b_p \neq b_s$. In practice, when one achromatic lens is used to focus the pump and signal beams inside the crystal it is difficult to reach

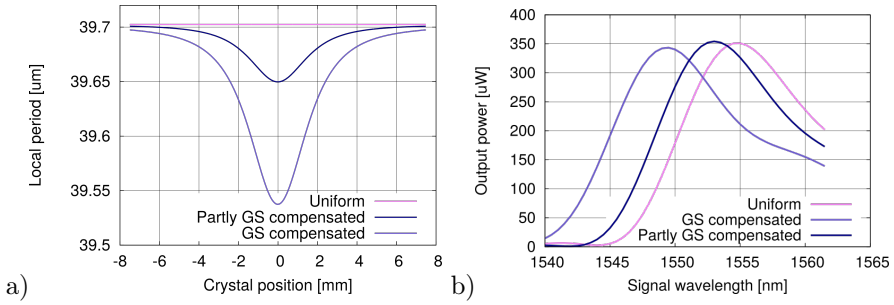

Figure 7: (a) Poling patterns for confocal beams. (b) Output idler power as a function of signal wavelength for the pump wavelength fixed at 1060 nm.

the case $\omega_{0P} > \omega_{0S}$ because of the lens material dispersion. The ray with the longer wavelength will be focused in a spot with bigger size. Also the waists will be shifted to each other. But if different lenses are used for separate pump and signal beams before combining together, any relation between $\omega_{0P}$and ω_{0S}can be obtained. We created a special setup with a possibility to focus 1.06 μm and 1.55 μm beams with different lenses to prove the calculations. The results of this experiment will be described later in part 4.7.

The second possibility of the DFG efficiency enhancement described in this work is engineering of QPM devices with a special aperiodically poled structure [52–56]. The uniform periodic structure is ideal to compensate the phase mismatch $\triangle k = 0$ between plane interacting waves. In the case of focused beams, the Gouy phase shift prevents the perfect phase matching. Aperiodic poling of the nonlinear crystals can partially overcome this problem. Extending the theory of Boyd and Kleinman, Major [57] derived the condition for compensation of the negative effect of the Gouy phase shift

$$\kappa(\zeta) = \frac{\cos(\zeta\sigma + \arctan[\zeta])}{|\cos(\zeta\sigma + \arctan[\zeta])|} \tag{17}$$

where $\zeta = {}^{z}/_{z_R}$, $\sigma = \triangle k{}^{b}/_{2}$ $\kappa(\zeta) = \pm 1$ and represents the periodicity changing of the nonlinear coefficient ($+d$ or $-d$). Calculated lengths of inverted domains for a non-uniform pattern according to this equation are following: $\Lambda_{KTP}(x) = -6.47{\cdot}10^{-8} \exp\left(-\left({}^{x-7.5{\cdot}10^{-3}}/_{2.9{\cdot}10^{-3}}\right)^2\right) + 35.81{\cdot}10^{-6}$ for KTP, and $\Lambda_{KTA}(x) = -7.95 \cdot 10^{-8} \exp\left(-\left({}^{x-7.5{\cdot}10^{-3}}/_{2.9{\cdot}10^{-3}}\right)^2\right) + 39.7 \cdot 10^{-6}$ for KTA crystals. We also investigated the pattern where Gouy-shift (GS) was partly compensated, i.e. only ${}^{\delta\zeta}/_{\pi}$ is compensated. For the KTA crystal all three patterns are presented in Fig.7(a). In figure 7(b) there are calculated output powers for these patterns. The calculation of such type of structures was done by Fourier transform beam propagation method (FT-BPM) and presented by our team in [C8] and [C7]. It also allowed us to prove and compare the results obtained with the FEM method. The output power was calculated for the constant pump wavelength (1060 nm) while varying the signal wavelength. The pump and signal beam

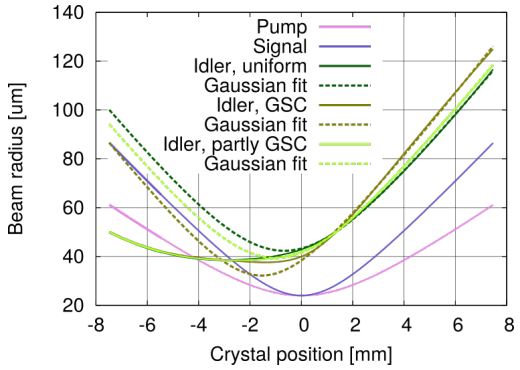

Figure 8: Beam radii for pump, signal and idler calculated with FDTD-BPM [C8] for uniform, Guoy-shift compensated (GSC), and partially GSC patterns.

waist had the same size of 24 μm and the waist positions were in the center of the crystal. Analyzing these results, we can see that the uniform pattern provides the maximum power for the signal wavelength longer by approximately 5 nm than the wavelength of 1550 nm obtained from the condition $\triangle k = 0$. On the other hand, the Gouy phase shift compensated structure works well for the focused beams with the wavelengths obtained for the plane-waves interaction (1060 and 1550 nm). But the best result of 354 μW is observed for the non-uniform partly GS compensating pattern for the signal wavelength of 1553 nm. The efficiency enhancement is $\sim 1\%$.

We also inspected the beam radius and waist position of the idler beam throughout the crystal. These values were taken iteratively from the results of numerical simulation and presented in Fig.8. It can be seen that the idler beam had a non-Gaussian character and its radius evolved non-symmetrically along the crystal. Closer to the input side of the crystal beam radius varied only slightly. The tightest place, which we can link to the beam waist, is shifted to the input from the center. In the second half of the crystal, the idler beam was quite close to Gaussian beam approximation and differed only moderately for three poling patterns.

As we have seen from this chapter, the most appropriate crystal for our aim to create the mid-infrared tunable DFG source is KTP. Its low price allows us to carry out many attempts of the poling experiment keeping appropriate tunability and output power. For the purpose of comparison one more expensive isomorph KTA is also used. The efficiency of the DFG process can be improved by both the focusing conditions and optimal poling pattern. Therefore, photolithography masks with various poling patterns based on the numerical simulations are designed. That includes periods of 35.4, 35.6, 35.9, 36.1 μm and aperiodic structure described by function $\Lambda_{KTP}(x)$ for KTP crystals and periods of 39.8, 40.1 μm and aperiodic structure $\Lambda_{KTA}(x)$ for KTA crystal. The validation of our numerical models will be done in the experimental part of the thesis 4.7.

4 Experimental results

In this chapter various setups of the fundamental Yb-doped and Er-doped fiber lasers are presented. Fabrication of the periodically poled ferroelectric crystals is described in detail. Then the description of DFG sources based on PPKTP and PPKTA is given. In the end, the experiment to optimize the DFG process is presented.

All fiber lasers described in this part (excluding tunable diode laser 81600B from Agilent) were home-made. For this, Vytran® glass processing unit was used. This device is ideal for splicing of various types of fibers, producing fiber couplers and combiners, etc. During the operation with this workstation, the author gained invaluable experience in fusion splicing of fibers and fiber lasers fabrication.

4.1 Widely tunable fiber lasers

This part of the thesis is based on the author's work within the frame of the project MŠMT LD 14112/020041 Mid-Infrared Radiation Generation, Delivery and Applications and was presented in [C1]. During the research, the author was responsible for the Yb-doped fiber laser development (Er-doped fiber laser was already designed for some previous project), measurement the characteristics of the lasers, processing and analysis of the measured data.

4.1.1 Widely tunable Yb-doped fiber laser

Wide tunability of the fundamental lasers allows us to cover a wide spectral range in the mid-IR region. Investigation of the possible tunability of the Yb-doped fiber laser (YDFL) was started with a simple linear resonator. The YDFL setup is shown in figure 9(a). It is based on a ytterbium-doped polar-

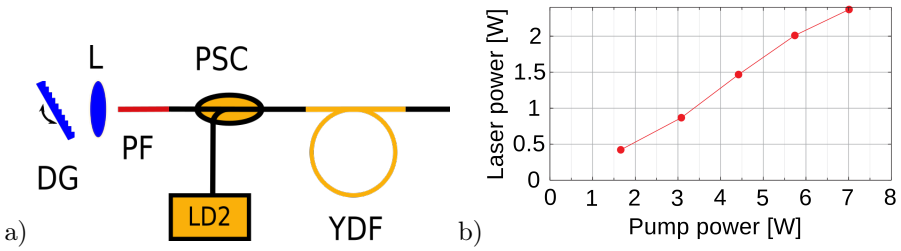

Figure 9: (a) Yb-doped fiber laser setup: DG - diffraction grating, L - collimating lens, PF - polarizing fiber, PSC - pump-signal combiner, LD - laser diode, YDF - Ytterbium doped fiber; (b) output power of the laser at 1072 nm.

ization maintaining (PM) double-clad fiber (Nufern, PLMA-YDF-10/125-HI-8) pumped by a high-power laser diode (LD) at 975 nm (Lumics, LU0975T090) by the means of a pump-signal fiber combiner (Optosun, PMPSC-1x2-980). The active fiber has a length of 3.5 meters. This length is enough to absorb almost

all the pump power. A 3 m long polarizing fiber (Thorlabs, HB1060Z) is used in the setup to enhance the polarization extinction ratio of the laser output. The laser has a resonator in the Fabry-Perot configuration with a diffraction grating (Thorlabs, GR13-1210) in a Littrow setup used as a wavelength selective element. The output coupler is formed by a perpendicularly cleaved fiber end with a reflection of about 3.5 percent. The laser is able to supply more than 2 W of continuous power at 7 W of the pump power (see Fig. 9(b)). The maximum output power was measured at the wavelength of 1072 nm.

The spectrum of the pump laser was measured with ThermoScientific Nicolet 6700 fourier-transform infrared (FT-IR) spectrometer. The line width of the pump laser at 1072 nanometers is in figure 10(a) and it is around 40 pm (∼10.5 GHz), what is larger than the resolution of the FT-IR spectrometer, which is equal to $1/8\text{cm}^{-1}$, or 15 pm for this wavelength range. The laser is tuned by rotation of the diffraction grating and covers a spectral range of 45 nanometers (Fig. 10(b)).

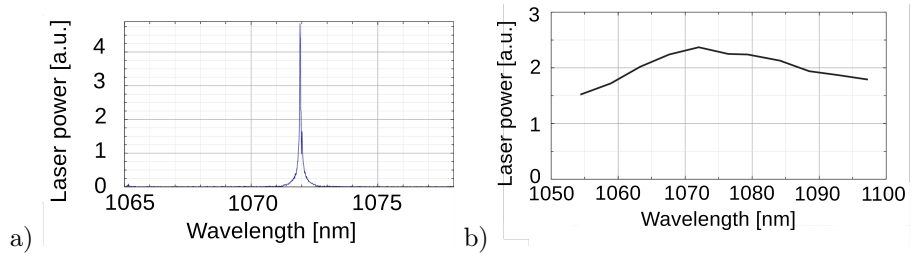

Figure 10: (a) Laser line of YDFL measured on FTIR, (b) spectral power of the laser in tuning range.

Ordinarily, utilization of the polarization-maintaining (PM) fiber components in lasers leads to more stable lasing. Despite the fact that the developed Yb-doped fiber laser contains only PM elements, the fiber had a tendency to self-damaging at the laser operation power higher than 1 W in the course of tuning. In our opinion it is a result of a self-pulsing or even giant pulse formation. As a solution to suppress these negative effects a master-oscillator power-amplifier (MOPA) laser configuration was chosen for the next design of the lasers. In such a configuration the master oscillator works at a power level of up to a few hundreds of mW, what is lower than the fiber's damage threshold, and all system is more stable.

4.1.2 Widely tunable Er-doped fiber laser

For the first experiment with the erbium-doped fiber laser (EDFL) at the signal wavelength range around 1550 nm the available laser with a sigma-configuration was used. The sigma-configuration allows to achieve a stable output polarization and prevent signal fading in a laser with a mix of polarization maintaining (PM) components and standard, non-PM components. This laser was developed early in our lab and the detailed description can be found in [58]. For the purpose of

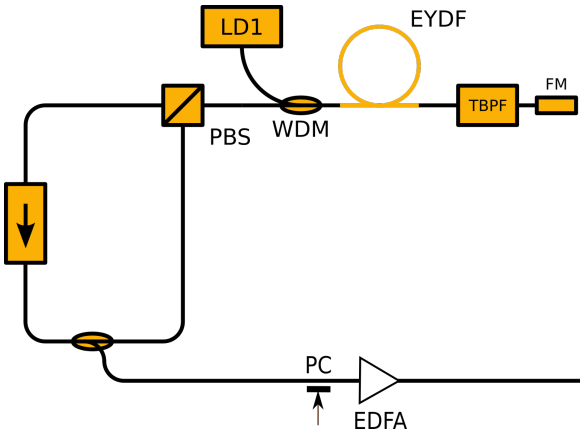

Figure 11: Er-doped fiber laser setup: FM-Faraday mirror, TBPF-tunable band-pass filter, EYDF-Erbium-Ytterbium-doped fiber, LD-laser diode, PBS-polarizing beam splitter,PC-polarization controller, EDFA-Erbium-doped fiber amplifier.

this work the laser was slightly modified. There is the composition of the signal laser in Fig. 11. This tunable Er-doped fiber laser has a MOPA arrangement. The master oscillator has PM elements placed in a fiber loop and connected by a polarizing beam splitter (Opneti, PBS-1x2-P-1550) with the remaining elements placed in a non-PM branch. The non-PM branch contains 10 m of an Er–Yb-doped optical fiber (Nufern, SM-EYDF-6/125-HE) backward pumped by a high-power laser diode at 975 nm (Lumics, LU0975T090) via a wavelength division multiplexer (Optosun, WDMC-1x2-980/1550). The birefringence of the non-PM branch is compensated for by a Faraday mirror (Thorlabs, MFI-1550-APC). The PM loop contains only an isolator (E-Tek, PIFI23AB11100) and a 50% output coupler (Optosun, CP-S-P-2x2-15-50/50).

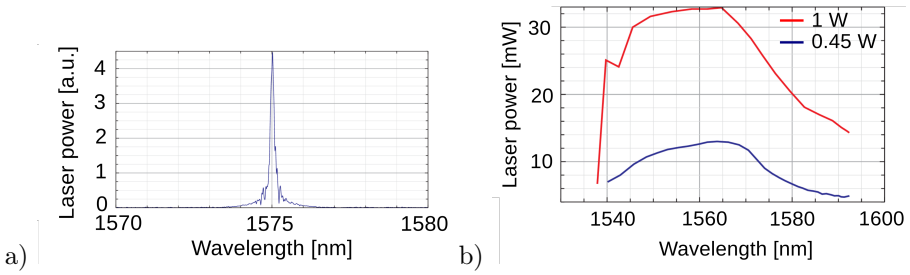

Figure 12: (a) Laser line of EDFL measured on FTIR, (b) spectral power of EDFL in tuning range for 0.45W (blue) and for 1W (red) of pump power.

The tunable band-pass filter (Koshin Kogaku, TFM-1550-S-FA) is used as a wavelength selective element. Fig. 12(a) shows the spectrum width of the signal laser at 1575 nm wavelength. The laser line is quite narrow and has the width of

around 20 pm (∼2.4 GHz). In Fig. 12(b) there are output power dependencies on the wavelength for two different pump powers of 0.45 W (blue curve) and 1 W (red curve). This sigma-laser covers a spectral range of 1540-1595 nm.

The laser signal is then amplified in a high-power amplifier (Keopsys, CEFA-C-BO-HP) to a level up to 2W. Expectedly, the laser itself has a very high power stability.

Using the MOPA configuration evidently increased the lasing stability and narrowed the laser linewidth. In turn the laser linewidth of the fundamental lasers will determine the difference frequency generator linewidth at the mid-IR range, which is related to the final resolution of spectroscopic device. Even for the device with a moderate resolution the linewidth should be at the sub-GHz level. The subsequent part of this chapter will be aimed at the laser line narrowing of the pump and signal fiber lasers.

4.2 Narrow-linewidth widely tunable fiber lasers

The following text is based on the results presented at [C10,C11] and author's talk [C9] and publication [P1]. In this part of work the author was responsible for lasers construction, measure, processing and analyzing of acquired data.

4.2.1 Narrow-linewidth widely tunable Yb-doped fiber laser

At first, a ring cavity fiber laser arrangement was utilized as a potential single-frequency operation configuration [59–61]. The Yb-doped fiber laser with the ring configuration was built on polarization maintaining (PM) components and fibers in order to achieve high stability and well-defined polarization. The laser consisted of 3.5 m of Yb-doped PM active fiber PM-YSF-LO from Nufern; a computer-driven narrowband tunable filter F with the central wavelength of 1060nm, tuning range of 100 nm, and FWHM of ∼0.1 nm (∼17.78 GHz) from WL Photonics Inc.; and a hybrid fiber-pigtailed optical component (Optosun, PMTIWDM-T1064/R980) that integrated a pump-signal combiner, a polarizing isolator and a 50 %-output coupler (see Fig.13(a)). A laser diode LD AC1409-0600-0976 from Gooch&Housego operating at a wavelength of 976 nm with maximum output power of 600 mW was used for core pumping of the Yb-doped active fiber. The ring laser was filter-tunable in a spectral range of 1020–1089 nm (see Fig.13(b)) and its linewidth measured by FT-IR was about 20 pm (∼ 3.53 GHz) at 1060 nm for the pump power of 500 mW (Fig.13(c)). Further, we tried to explore the laser behavior at various pump powers.

In this ring laser configuration, for the pump levels higher than 300 mW a fast detector (DET08CFC, Thorlabs) revealed pulsing with an irregular waveform on a long-time scale and pulsing with a period equal to the laser round-trip time around 33 ns on a short-time scale (see Fig.14(a)). We attributed the pulsings to a few-mode regime of the laser. But for the LD pump levels lower then 300 mW the CW regime was observed. Additionally, the fine spectral features of this laser in a CW regime were analyzed with the scanning Fabry-Perot interferometer (SA200-8B, Thorlabs). At the wavelengths range with the

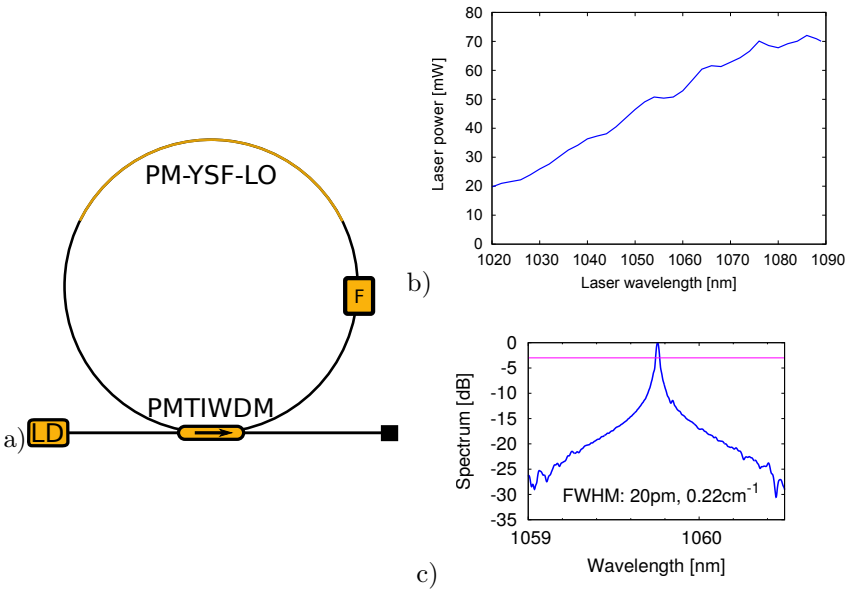

Figure 13: (a) Yb-doped fiber laser in ring configuration, (b) spectral power of the YDFL in tuning range at 500 mW of pump power, (c) YDFL linewidth at the filter position corresponding to 1060 nm.

higher laser power (1060–1090 nm) the measured linewidth of the laser was ∼1200 MHz and at the shorter wavelengths with lower laser power it was ∼600 MHz (see Fig.14(b)).

It is obvious, that the linewidth of the laser in ring arrangement in CW regime was about an order of magnitude narrower compared to the linear resonator described in chapter 4.1.1. The next step of this work was dedicated to the exploring of the various ring laser configurations for further narrowing of the laser line width.

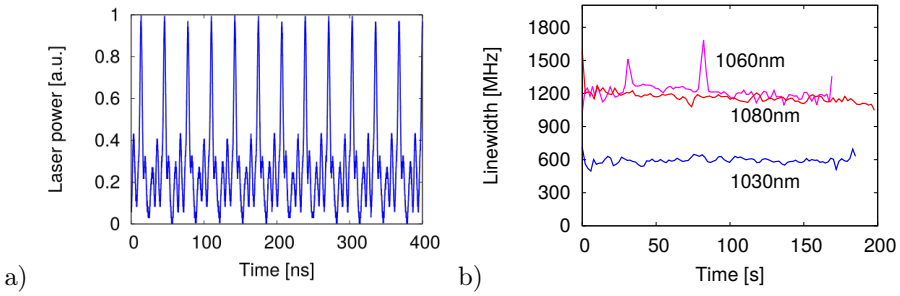

Figure 14: (a) Pulsing regime of YDFL in ring arrangement at the pump power of 500 mW, (b) laser linewidth in CW regime measured with scanning Fabry-Perot interferometer.

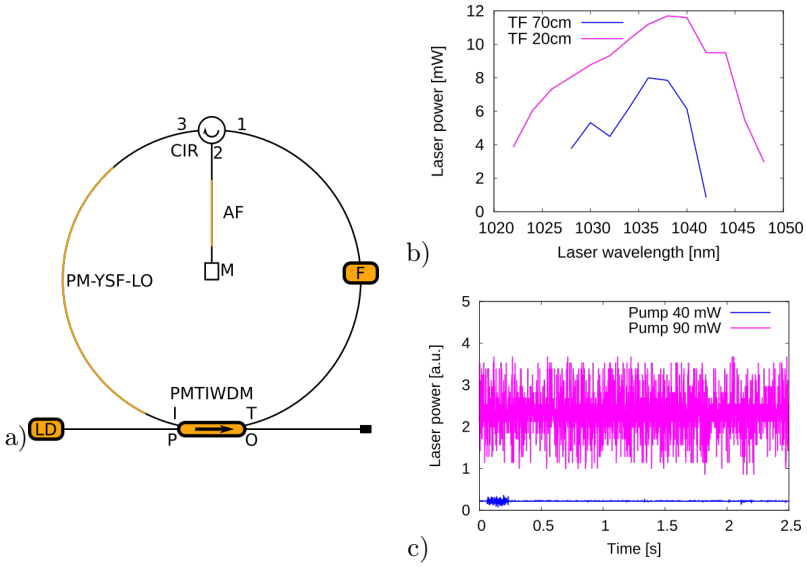

Figure 15: (a) Yb-doped ring fiber laser with tracking filter, (b) spectral power of the ring YDFL in tuning range at 300 mW of pump power for different lengths of active fiber (AF), (c) waveform from oscilloscope for ring YDFL at different pump levels.

Firstly, setup with a tracking filter [62] was examined. This configuration (see Fig.15 (a)) additionally included a circulator CIR (Optosun, PMCIR-3B-1064), a short length of the same Yb-doped unpumped active fiber AF and a mirror M (Thorlabs, P1-1060PMR-P01-1). The tracking filter was formed by a spatial hole burning originating from a standing wave in the unpumped segment of the active fiber. In this experiment two lengths 20 and 70 cm of the unpumped active fiber were used. The tuning range was significantly decreased due to the large loss imposed by insertion into the resonator of the circulator, the unpumped fiber, and the mirror (see Fig.15(b)). For very low pump powers, just above the threshold, the true CW regime with only rare fluctuations was observed. The laser linewidth measured at 1060 nm was around 100 MHz. For higher pump powers, the laser output waveform showed the same irregularities as for the fiber ring configuration (Fig.15(c)). Despite the narrower laser linewidth this laser was not exactly suitable as a fundamental source for widely tunable DFG due to a very limited tuning range.

The second approach for the laser line narrowing used the ring fiber resonator with a double-pass filter (see Fig.16(a)). This setup additionally included the circulator CIR, pigtailed mirror M, and narrowband tunable filter F placed between mirror and circulator. Light passed trough the filter two times and, in this case, an effective filter bandwidth decreased by approximately $\sqrt{2}$ ($FWHM_{DP} = FWHM/\sqrt{2}$). Within the operating range of the laser, the output power was only slightly reduced compared to the simple fiber ring laser because the active fiber was placed between the circulator and the output

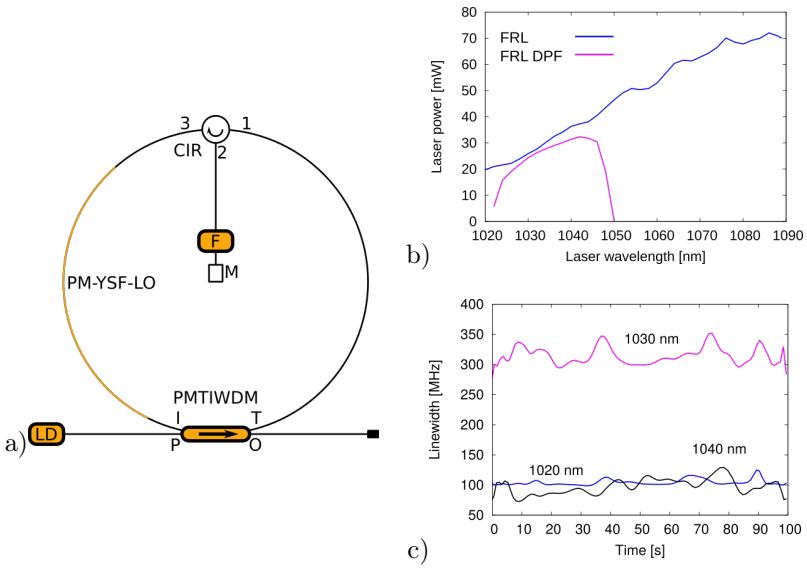

Figure 16: (a) Yb-doped ring fiber laser with double-pass filter, (b) comparison of spectral powers of ring YDFL with double-pass filter (FRL DPF) and ring YDFL (FRL) at 500 mW of pump power, (c) laser linewidth in CW regime measured with scanning Fabry-Perot interferometer.

coupler. However, as a result of large insertion loss of the circulator and another pass through the filter, the tuning range of the laser was strongly reduced. The tuning band was centered around the wavelength 1030 nm, which is a wavelength of maximum emission cross-section of the ytterbium fibers (see Fig.16(b)). This concept had really led to lowering the laser fluctuations. Quite stable regimes were observed for both the 1020-nm band and the 1040-nm band, while the fluctuations were present in a region around 1030 nm only (Fig.16(c)). The laser linewidth was almost one order narrower than for the ring configuration, but due to the short tuning range this laser also was not utilized in final setup.

The third attempt to narrow the laser linewidth was related to employment of a compound ring resonator. This fiber compound resonator, shown in Figure 17(a), needed an additional wideband fiber coupler to form a fiber cavity inside the main fiber ring. In our experiment 90/10 PM fiber coupler (Optosun, CP-PS-P-2x2-1064-10/90) was used and the the loop was built on 10% outputs. Both resonators are coupled and each of the resonators have their own set of resonances. The transmittance of the compound resonator decreases when a mode-hopping occurs and this has an effect on stability of the laser [63]. The spectral power of the laser was not affected too much by additional losses inside the coupler and the tuning range had almost the same width as for the ring cavity setup (see Fig.17(b)). As shown in Figure 17(c), the laser linewidth was significantly narrower with the compound resonator and for the low power wavelength range decreased by a factor of 12 as compared to the ring YDFL.

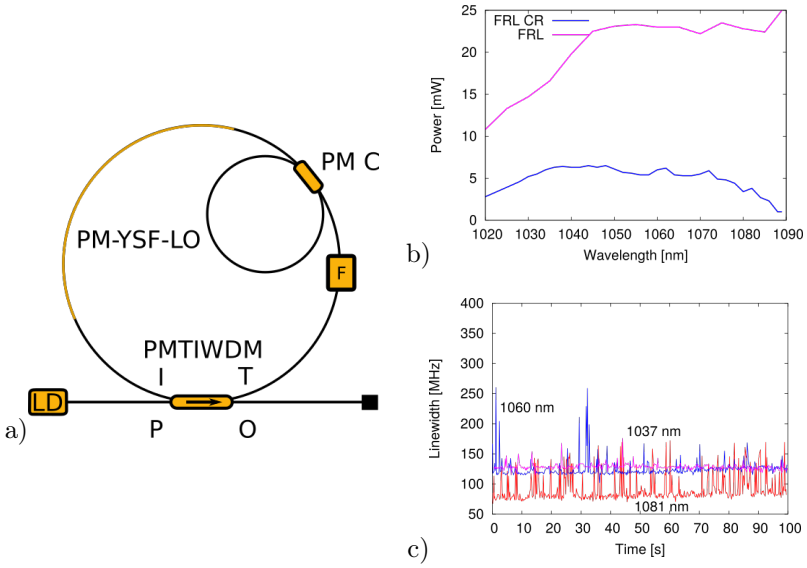

Figure 17: (a) Setup of Yb-doped ring fiber laser with compound resonator, (b) comparison of spectral powers of ring YDFL with compound resonator (FRL CR) and ring YDFL (FRL) at 300 mW of pump power, (c) linewidth of the laser in CW regime measured with scanning Fabry-Perot interferometer.

On the contrary, pulsings noticeably increased with the compound resonator and for the power level higher than 15 mW led to the damage at the amplifier stage. Despite the narrower laser linewidth, pulsations did not allow to use this configuration in the final prototype of DFG source.

4.2.2 Narrow-linewidth widely tunable Er-doped fiber laser

Er-doped fiber lasers in the same configurations, excluding configuration with the double-pass filter, were studied and very similar results to YDFL were obtained. The ring EDFL shown in Figure18(a) consisted of 3.5 m of Er-doped PM active fiber PM-ESF from Nufern; a computer-driven narrowband tunable filter F from WL Photonics Inc. with the central wavelength of 1550nm, tuning range of 100 nm, and FWHM of ∼0.1 nm (∼8.32 GHz); and a hybrid fiber optical component (Optosun, PMTIWDM-T1550/R980) that integrated a pump-signal combiner, a polarizing isolator and a 50 %-output coupler for the 1550 nm range. The active fiber was core-pumped by a laser diode LD AC1409-0600-0980 from Gooch&Housego working at the wavelengths of 980 nm. This laser was filter-tunable from 1520 to 1589 nm (see Fig.18(b)). The ring EDFL worked in the CW regime for the pump levels not higher than 300 mW and the measured linewidths in this regime for the various wavelengths were in the range of 300 MHz to 1200 MHz (see Figure18(c)).

The next tested configuration was the ring EDFL with the tracking filter

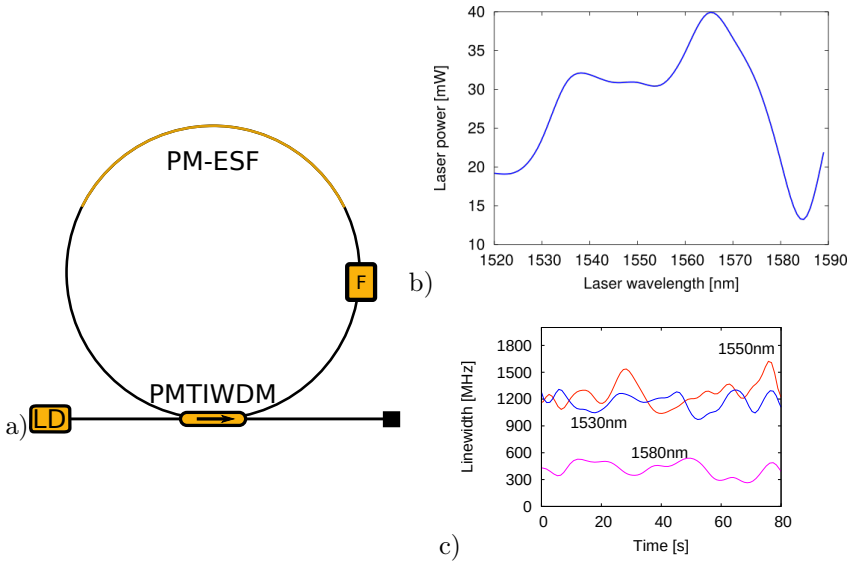

Figure 18: (a) Er-doped fiber laser in ring configuration, (b) spectral power of the EDFL in tuning range at 500 mW of pump power, (c) EDFL linewidth measured with scanning Fabry-Perot interferometer.

shown in Figure19(a). The setup was very similar to that of YDFL with the tracking filter and additionally incorporated a circulator CIR (Optosun, PMCIR-3B-1550), a 20-cm length piece of Er-doped unpumped active fiber AF, and a mirror M (Thorlabs, P1-1550PMR-P01-1). As it was already shown for the same configuration of Yb-doped laser, the output power was lower and the tuning range was shorter (see Figure19(b)). The CW regime was observed only for the low pump power near the threshold and the measured linewidths presented in Figure19(c) were in the range of 140–170 MHz.

The last tried configuration was the Er-doped fiber laser with a compound ring resonator. The fiber compound resonator, shown in Figure 20(a), included an additional 90/10 PM fiber coupler (Optosun, CP-PS-P-2x2-1550-10/90) to form a fiber loop inside the main fiber ring. The output power of the laser was not significantly decreased due to additional losses inside the coupler and the tuning range had almost the same width as for the ring cavity setup (see Fig.20(b)). Despite the noticeable (around 10 times) laser line narrowing, as shown in Figure 20(c), occasional pulsings in the ring compound resonator occurred even at the low laser power near 10 mW.

The research on different types of ring fiber resonators demonstrated significantly laser line narrowing especially in the compound ring resonators and lasers with double-pass filter. On the other hand, the presence of the circulator in the resonator had a detrimental effect on the tunability range of the lasers and the additional coupler led to the increased intensity pulsations. The choice of an appropriate laser configuration for the spectroscopic device is not only a trade-

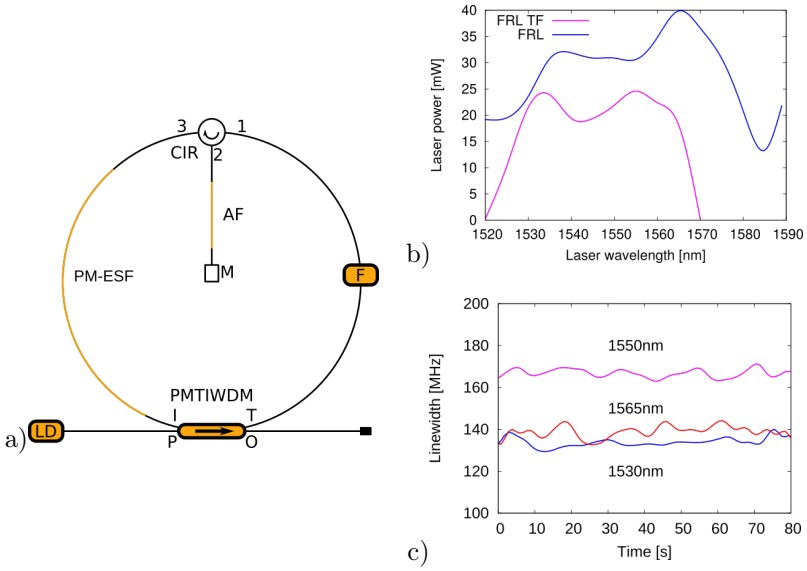

Figure 19: (a) Er-doped ring fiber laser with tracking filter, (b) spectral power of the ring EDFL with tracking filter in tuning range at 300 mW of pump power compared to ring EDFL, (c) laser linewidth in CW regime measured with scanning Fabry-Perot interferometer.

off between the wide tunability and laser linewidth, but it is also a question of device reliability. Simple ring configurations demonstrated wide working ranges of the lasers 1020–1089 nm and 1520–1589 nm for Yb-doped and Er-doped fiber lasers respectively. Along with adequate output power and low pulsing level these ring lasers were chosen as the fundamental sources for one of the future prototypes of mid-infrared DFG source. Despite the relatively wide linewidth of the lasers (~GHz) such a widely tunable mid-infrared source still can be used for low-resolution mid-IR spectroscopy.

4.3 Broadly tunable single-frequency fiber laser.

Here, the author report on a single-frequency ytterbium-doped fiber laser with a broad tunability developed in our lab. This laser was firstly mentioned in [C6] and described in detail in publication [P2]. To not completely repeat what was published by the author's coworkers, here we confine ourselves to the description of the work to which the author directly contributed, i.e. laser constructing and characterization.

As our previous research revealed, the fiber ring laser is a good choice for the laser line narrowing. The ideal case is a single-frequency laser, i.e., laser working in a single longitudinal mode (SLM). But such a task is not trivial because of a few distinctive features of fiber laser resonators. The gain of the active fiber is distributed in relatively long length (few dB per meter), as a result,

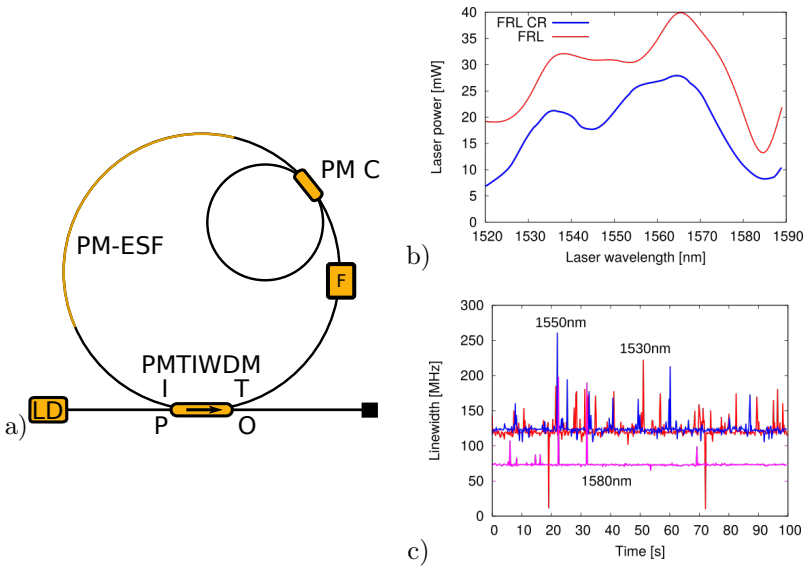

Figure 20: (a) Setup of Er-doped ring fiber laser with compound resonator, (b) comparison of spectral powers of ring EDFL with compound resonator (FRL CR) and ring EDFL (FRL) at 300 mW of pump power, (c) linewidth of the laser in CW regime measured with scanning Fabry-Perot interferometer.

the fiber resonator ordinary has a length of meters or even tens of meters. This gives a free spectral range (FSR) of the resonator in order of tens of MHz only. Additionally, the active fiber gain bandwidth is wide (tens of nm (∼10 THz) for Yb-doped fiber). The combination of these densely spaced longitudinal modes and large gain bandwidth results the fiber lasers operating in many longitudinal modes regime. On the other hand, using a fiber ring unidirectional resonator helps not only to double the FSR, and, as a result, reduces the number of the resonator modes, but also eliminates a spatial hole burning [64]. Employing the narrowband tunable filter, as was previously shown, can narrow the laser line bandwidth to the GHz level, what is still not enough for single mode generation. The fiber ring laser with the computer-controlled filter from WL Photonics Inc. works in a few longitudinal modes and demonstrates fluctuations in the output power. To build the single mode Yb-doped fiber ring laser we adopted the idea from [65], where an additional narrowband Fabry-Perot etalon (FPE) was used within the passband of the wideband tuning FPE. In our case, we employed a fiber ring resonator filter (FRRF), which is a fiber analogy of the Fabry-Perot resonator (FPR) [66]. This helped not only maintain the all-fiber configuration, but also eliminate the back reflections from FPE and, as consequence, does not need extra optical isolators. SLM selection principle described above is more clearly represented in Fig.21.

The laser setup with such a filter is shown in Fig.22. It is based on the ring fiber laser with 1.45 m of Yb-doped active fiber (Nufern, PM-YSF-HI) core-

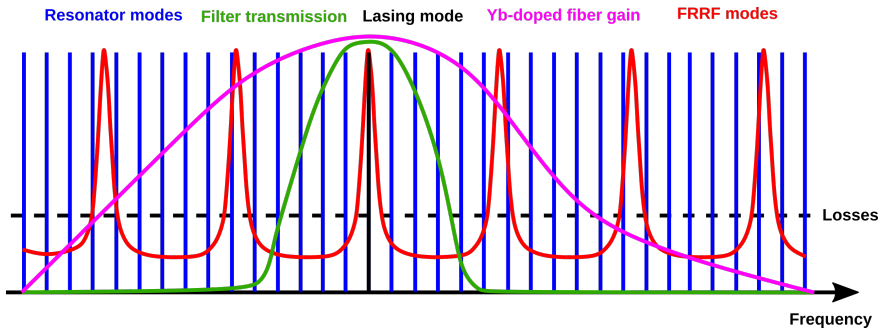

Figure 21: Schematic representation of the longitudinal mode selection using FRRF.

pumped by the laser diode with the stabilized wavelength at 976 nm (Gooch&Housego, AC1409-0600-0976) through the hybrid fiber optical component (Optosun, PMTIWDM-T1064/R980), which also includes a polarizing isolator and a 10 %-output coupler. The tunable grating filter from WL Photonics determines the fiber laser wavelength. All components and fibers used in the laser are polarization maintaining. In order to achieve the SLM regime, the FRRF is included to the resonator. The FRRF comprises two 2×2 wideband fused fiber couplers C_1, C_2 (Optosun, CP-PS-P-2x2-1064-95/5) with a split ratio of 95:5. The derived transmission function of the FRRF [67] can be written as

$$T = \frac{T_1 T_2}{1 + R_1 R_2 - 2\sqrt{R_1 R_2}\cos(knL)},$$

where T_1, T_2 and R_1, R_2 are the cross- and bar-coupling coefficients of the couplers, L is the total length of FRRF, $k = 2\pi f/c$ is a propagation constant, f is the signal frequency, c is the speed of light, and n is the effective refractive index of the laser mode in the FRRF. It is to be noted that a small difference in the coupling coefficients of the couplers T_1, T_2 significantly affects the peak transmission of the FRRF. We purchased three couplers of the same type and selected two of them based on the similarity of their spectral transmittance within the range of interest. The calculated peak transmission of FRRF with the assumption that there are no losses in the fiber and couplers, i.e., $R_{1,2} = 1 - T_{1,2}$, is presented in Fig.23(a). The calculated finesse of the filter changed from 50 to 25 from shorter to longer wavelengths. The ring fiber laser based on the FRRF was tunable in a spectral range of 1023-1107 nm (see Fig.23(b)) at the maximum allowable for the optical hybrid component pump power of 300 mW. For comparison, the average output power of fiber ring laser without FRRF is also provided.

The next step of the work was to investigate the mode structure of the designed laser. For this, a scanning Fabry-Perot interferometer (SFPI) SA210-8B from Thorlabs with the FSR of 10 GHz and a resolution of 67 MHz was used. Data from the SFPI detector were recorded employing a digital sampling

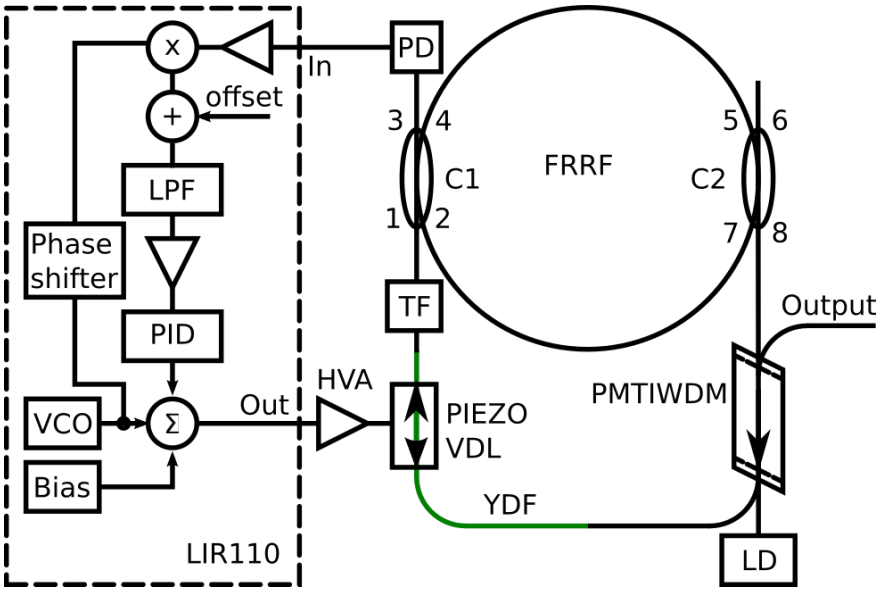

Figure 22: Setup of the fiber laser with the fiber ring resonator filter: PMTIWDM, hybrid component integrating polarizing isolator, output coupler, and wavelength division multiplexer; LD, pump laser diode; YDF, ytterbium-doped fiber; VDL, piezo-driven variable delay line; TF, tunable grating filter; C1,2, couplers; PD, photodetector; LPF, low-pass filter; PID, proportional-integral-derivative controller; VCO, voltage-controlled oscillator; FRRF, fiber ring resonator filter.

oscilloscope (Agilent, Infiniium 54855A). Further analysis revealed that the laser operates in the SLM regime, but the laser line is hopping between the longitudinal modes of the FRRF within the time intervals on the order of seconds. Figure 24 shows the stability of instantaneous frequency. The mode hopping in multiples of 198 MHz which corresponds to the FSR of FRRF occurs regularly on time scale of seconds. Excursion of the instantaneous frequency can be as large as 7 GHz. These sudden frequency changes do not allow to use this laser in the high-resolution spectroscopy where the absorption lines have the width of ∼MHz.

To prevent the mode hopping an active stabilization of the laser resonator length was proposed. A piezoelectric chip was glued to the active fiber to create a variable delay line (VDL, see the Fig.22) and kept the main resonator length in the resonance with the FRRF. This fiber stretcher is a cheap element with a low insertion loss in comparison with phase modulators. When the length of the laser resonator is in the resonance with the FRRF, the signal at the port 3 (see Fig.22) reaches the minimum and this can be used as an error signal. Sinusoidal modulation with a small amplitude and frequency of 360 Hz superposed with the bias voltage is applied to the fiber stretcher. Periodically stretching of the fiber creates a frequency modulation, which is converted into an

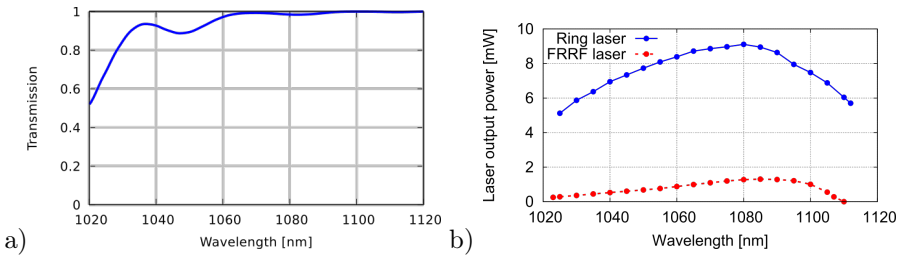

Figure 23: (a) Peak transmission of the FRRF, (b) output powers of the fiber ring laser and fiber ring laser with FRRF at the pump power of 300 mW.

amplitude modulation at the port 3, then demodulated in the lock-in regulator (Toptica, LIR110), amplified in a high-voltage amplifier, and applied as a bias voltage to the piezoelectric stretcher. In the presence of the feedback, the mode hopping disappeared and the laser frequency was stabilized at the central position (see Fig.24). The laser linewidth was evaluated using a coherent delayed self-heterodyne interferometer and was 11.7 kHz. This measurement is described in detail in [P2] and is not presented here because of only partial participation of the author in the measurement.

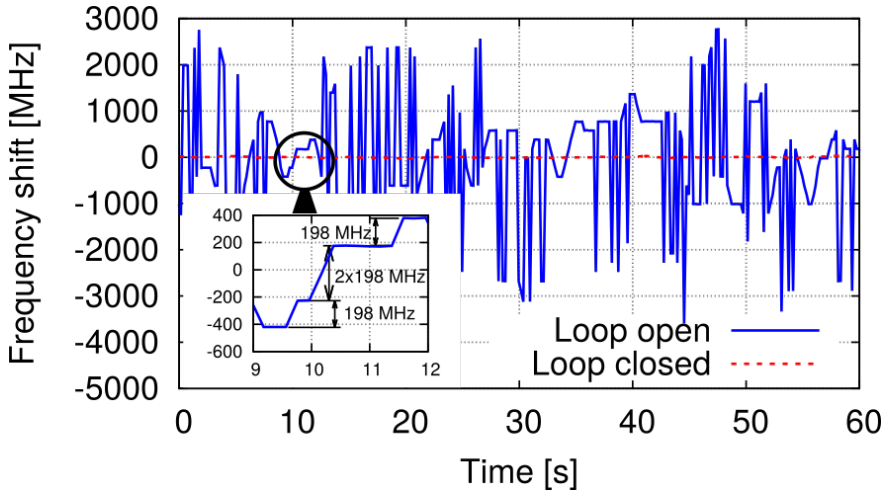

Figure 24: The shift of instantaneous frequency of the fiber laser with FRRF with opened and closed feedback loop.

The developed broadly tunable single frequency fiber laser is ideal for the panoramic absorption spectroscopy with a high resolution. In this section we also showed that the creation of the laser with a narrow line is a difficult task. As a starting point, the ring resonator configuration incorporated with the tunable narrowband grating filter allowed to build the widely tunable fiber laser with the linewidth of $\sim$ GHz. This laser still worked in a few modes regime. Using more

narrowband selective element in a form of FRRF made the laser to operate in the SLM regime. But external influences like temperature fluctuations, optical table vibrations, fluctuation of the laser diode pump power, etc., caused the mode hops. Using the feedback loop for the active stabilization of the resonator length resulted in the creation of the single frequency laser tunable in a range of 1023–1107 nm without the mode-hopping and with the laser linewidth of ∼11.7 kHz.

4.4 High power fiber amplifiers

This subsection describes the design and main characteristics of the fiber amplifiers working in 1060 nm and 1550 nm ranges. The majority of research described here was made by the author and was included to works [C9,C10,C11,P1]. As mentioned in the beginning of the subsection4.1.1 the constructed lasers have MOPA configuration. This is the most popular approach to power scaling. The signal from the master oscillator is amplified to an appropriate power level in the amplifier stage. The master oscillator in turn can produce signals of the relatively low power but with the narrow spectral width and good temporal stability.

Both amplifiers are built with PM fibers and components and have high-power isolators at the input to prevent damaging of the master oscillators. Laser radiation from the tunable YDFL, as presented in Figure25(a), goes through the isolator (Optosun, HPMIS-1064) to 6-m long double-clad large mode area active fiber with a geometry 10/125 μm (Nufern, PLMA-YDF-10/125) cladding-pumped by a high-power multimode LD working at 915 nm (Focuslight Technologies Co., Ltd., FL-FCMSE55-25-915) by means of pump-signal combiner (Optosun, PMPSC-2-F).

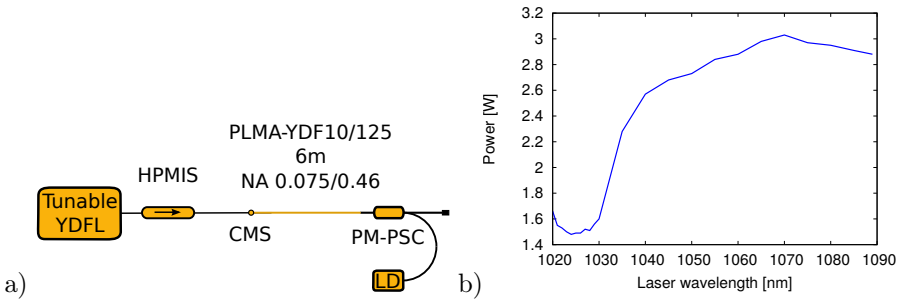

Figure 25: (a) Ytterbium-doped high power amplifier and (b) tuning curve of the YDFL MOPA.

The length of active fiber was chosen using a rule of thumb when a total pump absorption of around 10 dB. The residual pump light was removed from the active fiber using a homemade cladding mode stripper (CMS). We used the counter-propagating pump, where the pump and signal light are propagating in an active fiber in the opposite directions, because the co-propagating pump

setup demonstrated a tendency to self-damaging at the laser operation power higher than 1.5 W. In the whole tuning range the highest output power of 3 W after the amplifier was achieved near the wavelength of 1070 nm (see Fig.25(b)).

In the case of the Er-doped fiber amplifier presented in Figure26(a) the laser radiation from the tunable EDFL goes through the isolator (Optosun, HPMIS-1550) to 12-m long Er/Yb-doped double-clad active fiber with a geometry 6/125 μm (Nufern, PM-EYDF-10/125) cladding-pumped by the similar high-power multimode LD from Focuslight working at 915 nm by a pump-signal combiner (Optosun, PMPSC-2-F-915/1550). The Er-doped fibers co-doped with Yb^{3+} ions allow increasing the output power extracted from the amplifier by improving the pump absorption near 915-nm band where high-power multimode laser diodes are available. The unabsorbed pump was removed from the fiber by a cladding mode stripper (CMS), which is formed by a fiber splice placed in a drop of high refractive index adhesive (Thorlabs, NOA61) so the light propagated in the cladding is radiated out from the fiber. For this amplifier, the co-propagating pump setup demonstrated a stable and reliable operation. The signal from the tunable Er-doped ring fiber laser was amplified to a power level of ∼0.4–1 W and presented in Figure26(b).

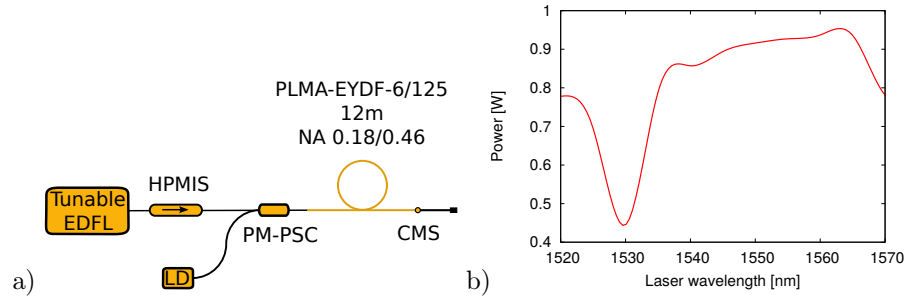

Figure 26: (a) Erbium/Ytterbium-doped high power amplifier and (b) tuning curve of the MOPA.

The high power fiber amplifiers described above work well with the CW ring fiber lasers, which have relatively broad linewidth of ∼1000 MHz. In case of operation with very narrow spectral lines laser (see Section 4.3) CW high power fiber amplifiers have some limitations. The first limitation is related to an amplified spontaneous emission (ASE) for operating at the wavelength far from the maximum gain wavelength. For example, in one-stage Yb-doped fiber amplifier (YDFA) at the high pump level the power of ASE can be even higher than the power of the signal with a wavelength far from the gain maximum at 1030 nm (see Fig.27(a)). This problem can be solved by using two-stage amplifiers setup with the lower pump powers. Moreover, the first stage can be changed by a semiconductor optical amplifier. As we shown in [C2,P3], the semiconductor optical amplifiers have very flat spectral gain and can be used in broadly tunable fiber laser avoiding ASE at the maximum gain wavelength. Our setup included the fiber pigtailed semiconductor optical amplifier (SOA-

1060-90-PM) from INNOLUME as a first stage. The second stage was the fiber amplifier with the similar setup presented in Fig.25(a), but with the length of the active fiber of 70 cm and the pump power limited to 500 mW. As can be seen from Fig.27(b), the ASE at 1030 nm was suppressed and there was not so big difference in output powers for the various wavelengths in the tuning range of the laser.

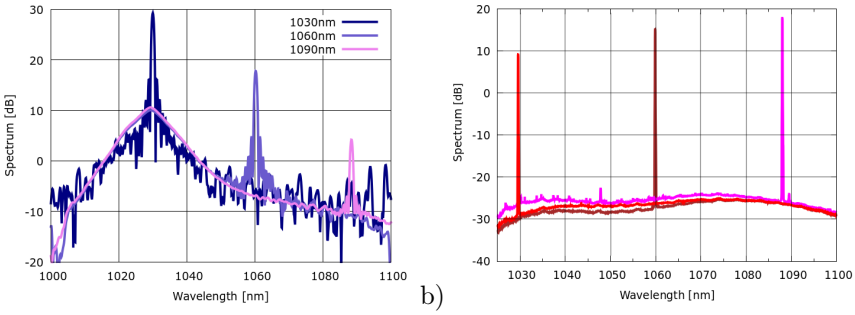

Figure 27: (a) Spectrum of YDFA at various wavelengths. (b) Spectrum of two-stage SOA and YDFA at various wavelengths.

The second limitation of the CW high power fiber amplifiers is related to a non-linear effect of stimulated Brillouin scattering (SBS) in fibers. If the signal has a bandwidth narrower than the Brillouin linewidth (∼50 MHz), the electrostriction creates an acoustic wave in fiber. This results in a back scattering of the signal and limits the amplifier output power [68]. In our two-stage fiber amplifier the input signal power was not high (up to 10 mW) and a relatively short special large mode area fiber from Nufern was used. These factors helped to minimize SBS effect.

The beams from Yb- and Er-doped fiber amplifiers are combined in a wavelength-division multiplexer. The output pigtail of the multiplexer is equipped with an angle-polished connector to suppress the reflections from the end facet of the fiber. After the multiplexer the fundamental beams go to a nonlinear head of the device. This part of the first mid-IR laser source prototype with the nonlinear crystal will be described below in Section4.6.

4.5 PPKTP and PPKTA fabrication

The first periodically poled structures in KTP crystals were fabricated in 1990 using an ion-exchange process. Such a structure had a form of a waveguide and was used for a blue light generation [69]. This fabrication method is relatively difficult, very demanding to processing conditions, and did not work well for power levels higher than a few milliwatts. The second method of production of periodically poled structures in KTP was demonstrated in 1993 [70]. Gupta with colleagues used e-beam scanning of the *-c* face of a 1-mm-thick KTP crystal to create periodical domain reversal with 20 μm periodicity. For the equal width

of inverted and uninverted domains on the -c face of the crystal, the ratio of the corresponding domains widths on the opposite $+c$ face was 3:2. As a result of such inaccuracy, this method did not become very popular.

The most popular method for fabrication of the KTP crystals with a domain periodicity is an electric field poling process, which was realized in 1994 by Chen and Risk [71]. The main idea of the method is applying the high voltage electric field between $-c$ and $+c$ polar faces of the nonlinear crystal covered by metal electrodes. One of these electrodes represents a periodical micrometer-scale structure with an appropriate duty cycle. As can be seen in figure 5, which represents the DFG power calculated for 1060 nm and 1550 nm fundamental wavelengths, the size of a periodical pattern inside the crystal has a critical influence on the nonlinear conversion efficiency. Even a small error in periodicity, such as 100 nm, can cause power reduction by $\sim$40% (see Fig.5).

Basically, there are two methods of the electric field periodical poling process of KTP crystals. The main difference between these two approaches is that the poling process goes at different temperatures. The most commonly used method is a room temperature poling method which needs the crystals with relatively low ionic conductivity of $\sim 10^{-6} - 10^{-7}$S/cm, and is thus more suitable for $LiNbO_3$. On the other hand, more price-attractive KTP and its isomorphs can achieve the mentioned conductivity levels at lower temperatures [72]. At our laboratory we use low temperature technique for the fabrication of periodic domain structures in KTP and KTA crystals. Single domain z-cut KTP and KTA crystals 16.5 mm long, 12.5 mm wide and 1 mm thick ($x \times y \times z$) with polished xy planes and polished to optical finish yz facets were purchased from CRYSTECH. Inc for further QPM devices fabrication.

The author of this thesis contributed to the redesign of available but not being used for some time technology of periodic poling of the crystals at ÚFE. Specifically, in the recommencement of Photoresist Microposit S1818 process and high voltage electric field poling process. Although the photolithography technique is well known and some information about electric-field poling can also be found in the literature, the practical implementation of the fabrication of periodically poled KTP and KTA crystals is quite tricky. All steps of the process described in this section were done by the author and the results presented in [C10,C11,C1,C9,C8,P1,C7] were obtained using periodically poled crystals fabricated at ÚFE.

4.5.1 Cleaning process

First of all, before any electrode deposition on xy planes, the crystals acquired from the manufacturer must be cleaned. During the cleaning procedure contaminants with the submicron size must be removed from the surfaces parallel to xy plane (see Fig.2) to obtain high quality domain pattern in the crystal. We use a common cleaning procedure [73]. It is strongly recommended to clean the samples in a cleanroom facility. Before employing any cleaning technique, dust and other loose contaminants usually should be blown off with compressed nitrogen gas. Then the crystal surfaces are cleaned with the acetone and special

optical wipes or cotton-tipped applicators to remove any organic materials, such as skin oil or photoresist residues. After that, the sample is rinsed with a de-ionized (DI) water for at least 30 seconds and 30 seconds with isopropyl alcohol (IPA) thereafter to neutralize the ionic dust and remove the light grease. The cleaned crystal is dried by blowing with nitrogen and placed into an etching machine for a plasma dry etching with oxygen for 8 minutes to rest assured that the majority of the organic contaminants are removed from the crystal surfaces. In case of a hardened grease or insoluble contamination on the samples, ultrasonic cleaning into acetone can be applied. The cleaning process is a decisive process for all subsequent QPM devices manufacturing steps.

4.5.2 Photoresist deposition

To produce the periodically patterned electrode on one of the polar faces of the crystal conventional photolithography technique is used. A positive resist Shipley Microposit S1818G2 is spin coated onto $-$c-face at 3000 rpm speed for 30 seconds to obtain the photoresist layer thickness $\sim$2.5 μm (spin coater Laurell, ws-650mz-23nppb). This thickness is enough as isolation during applying a high-voltage electric field up to 10 kV. After the substrate has stopped spinning, it is better to let it sit for 15-20 sec for the photoresist to firm up, then transfer the crystal to an oven (Javoz, 25020) for softbaking at 90 °C for 30 minutes or on a hot plate (Witeg, HP-20D) at 120 °C for 1 min (it is observed that after 1 min of softbaking at a hot plate the photoresist is more sticky and can cause the mask defects). The thickness of the photoresist was measured on a test sample on a 3D optical surface profiler ZYGO NewView™ 8000. It was found that the thickness changes from 2.3 μm to 2.8 μm from the central region to the edge. To get rid of such a high photoresist thickness irregularity over the substrate an edge bead removal with acetone is required.

It is worth mentioning that the resist was spun onto $-$c-face of the crystal because it is difficult to distinguish any difference in terms of the domain nucleation density and domain wall propagation features in the crystals between placing the periodic electrode onto the $-$c and $+$c polar faces [74].

4.5.3 Exposure of photoresist

After the soft bake procedure, the photoresist S1818G2 needs to be exposed through a mask with the UV light. In Figure28(a) there is a drawing of one of typical masks we use for QPM devices fabrication. The masks we fabricated by Photronics, Inc based on our design. The quartz substrate is covered with the chromium layer and patterned by e-beam lithography method with an appropriate period. For the exposure of KTP and KTA crystal samples we use KARL SUSS MJB3 UV400 Mask Aligner equipped with 400nm exposure optics and Hg arc lamp in soft contact mode. In this mode, the substrate is held by a vacuum chuck during exposure and contact pressure is applied only through a spring force. The sample is exposed with the dose of 150 mJ/cm^2 for 43 seconds and then placed on a 115 °C hotplate for 60 seconds. We did

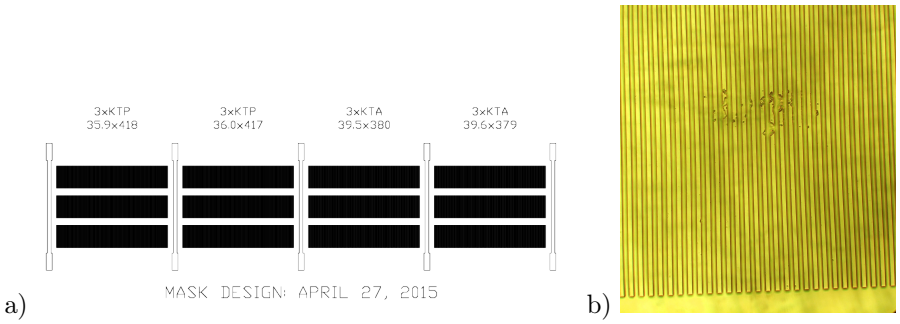

Figure 28: Photolithography mask for use with KARL SUSS MJB3 UV400 Mask Aligner (a). Defects on the mask at the periphery region.

not observed any significant differences in the quality of photoresist patterns with and without this post-exposure bake process. Due to diffraction and light scattering the best achievable resolution for this technique is ∼2 µm. With time, the resolution of the process can be also affected by appearing mask's defects (see Fig.28(b)), but some defects are allowed if they are at the periphery region.

4.5.4 Development of photoresist grating

For the development process we use Microposit 319 ready-to-use developer at the room temperature. The crystal with exposed photoresist is immersed in the developer for 45 seconds with gentle agitation. Then the wafer is rinsed with DI water for at least 30 seconds and dried with nitrogen with the gas flow in the direction of the pattern stripes. After that, to harden the photoresist structure, the wafer is hard-baked on a hotplate at 110 °C for 90 seconds. During the poling

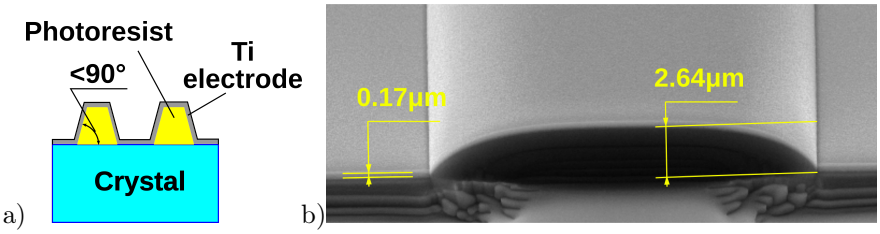

Figure 29: Photoresist profile with shallow angles $<90^0$ (a). Cross-section side view of 2.64 µm high photoresist stripe covered with Ti (b).

process the photoresist stripes work as an insulator for the patterned electrode. To cover this periodical structure continuously with metal it is necessary to have shallow resist angles ($<90^0$), as shown in Fig.29(a)). For our masks with a fill factor of 50%, the resist sidewall angle can be easily controlled by the development time in the range from 40 to 60 seconds (for longer time the angle is lower). In Figure29(b) there is a cross-section side view of 2.64 µm high

a) 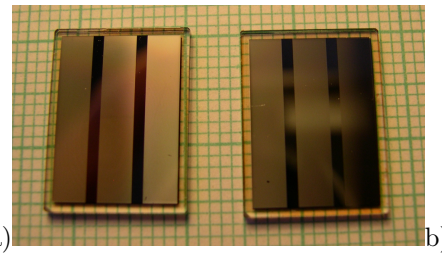 b) 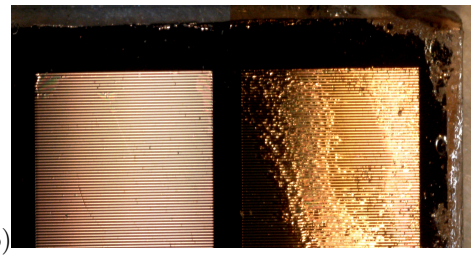

Figure 30: (a) KTP and KTA crystals with Ti electrodes and (b) detailed photo of the good (left) and bad-quality electrode (right).

photoresist bar obtained by scanning electron microscope (TESCAN, LYRA3). The edges of the upper plane are rounded because of the thermal softening of the developed resist structure during the hard-baking.

4.5.5 Electrode deposition

The next step is covering the photoresist layer with the Ti electrode. KTP and KTA crystals were covered from both sides with 100–200 nm of titanium film evaporated in a vacuum chamber (see Fig.29(b)). In order to cover sidewalls of the photoresist strips by metal, the crystal holder is rotating during the electrode deposition. This ensures a good electric contact with the high-voltage electrode. Figure 30(a) shows the good-quality Ti electrode on both crystals, for a comparison there are also a detailed photos (b) of good-quality pattern covered with Ti film (left) and bad-quality electrode Ti electrode (right) due to nonuniform photoresist thickness at the edge region.

4.5.6 Electric field poling

Electric field poling is one of the most important steps in QPM devices fabrication. At our institute, as mentioned earlier, we use the low temperature poling method [72] which reduces the ionic conductivity of KTP and KTA crystals by a few orders of magnitude. Using a three stage Peltier element, we are able to cool the crystals to a temperature of 230 K. Of course, it also has disadvantages as a required vacuum camera, cooling elements and drivers, higher poling voltage, but it allows us to control the poling process much easier than at room temperature, where strong ionic current screens the poling current. The schematic setup of the poling system is depicted in Figure 31.

The sample with the deposited electrodes is positioned inside the vacuum chamber as it is shown in Figure 32. After reaching the vacuum $\sim 10^{-5}$ mbar we can start to cool the crystal down to the temperature of 230 K. As the temperature controller has a PID regulator it ordinary takes ∼15 minutes to stabilize the temperature. After that, the crystal is poled by applying an appropriate number of electrical pulses. High-voltage amplifier (Trek, 20/20C) is driven from the AG4151 (OWON) generator which is set to generate electrical pulses 900 μs

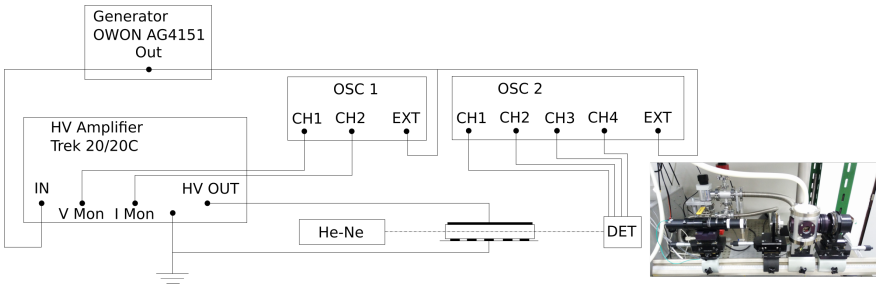

Figure 31: Schematic of electric field poling system. In inset is a photo of the vacuum chamber and poling control system.

long, with 150 μs leading and trailing edges. Nucleation of the domain inversion starts between the electrodes when a HV external electric field is applied to the sample. The nucleated reverse domain tips propagation and their sideways merging form a periodic domain structure. When all domains in the electrodes region are inverted, the external electric field should be switched off to avoid an overpoling. A spatial structure inhomogeneities in KTP and its isomorphs

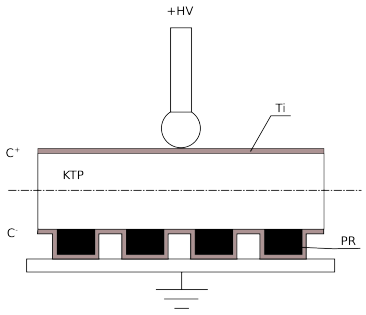

Figure 32: Crystal position inside the vacuum chamber.

make a poling hardly reproducible. For this reason, the monitoring process is extremely important to obtain good poling results. At low temperature poling process the lower conductivity allows us to monitor the current through the poling circuit to determine the progress of the poling and to find the right numbers of the pulses for when it is complete [33]. For better poling control the optical monitoring is using as well.

4.5.7 The poling process monitoring.

The construction of our vacuum chamber provides the possibility to use simultaneously monitoring methods with the current control and the transverse electro-optic effect in the crystal under the voltage [75]. This second method utilizes time-dependent changes in the polarisation-state of a He-Ne laser beam (see Fig. 31) while it propagates through the crystal during poling. The voltage

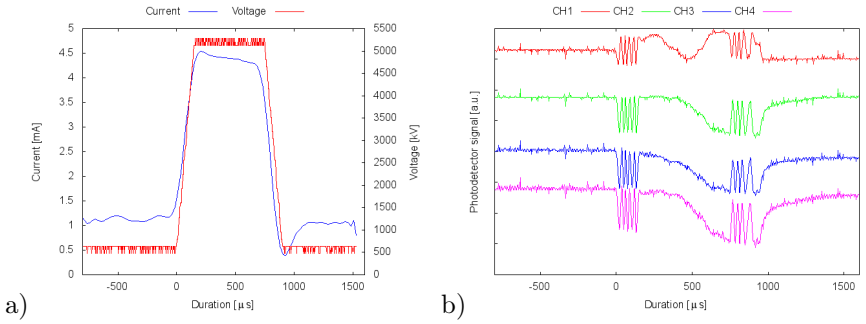

Figure 33: (a) Voltage and current through the KTP crystal during poling, (b) oscilloscope traces during applying voltage.

pulse up to 5 kV is applied (see Fig. 33(a)), the poling current depends on the crystal conductivity and ordinarily does not exceed 10 mA. Ordinary 3-4 pulses not higher than 5 kV are enough for good results for KTP, and $\sim$ 6.5 kV for KTA. The oscillogram of the normally running poling process from the optical trace is in Figure 33 (b). The electro-optical effect itself is clearly seen during the rising and falling edges of the applied voltage pulse, and in the middle of the pulse, where the voltage is constant, the polarization state will change only if the crystal is being poled. These changes correspond to the intensity oscillation on the detector and help to decide when to stop applying voltage. The monitoring system has 4 channels uniformly distributed by the width of the crystal to increase the probability of overlaying the grating region with the line detector. We can see from the figure 33(b) that He-Ne laser light goes through the periodic pattern at the area corresponding to the channels 2,3,4 of the detector. The rest channel 1 does not overlap with the patterns and represents only electro-optical effect. When the changes in the intensity of transmitted He-Ne light disappear, it is evidence of the end of poling (see Fig. 34). In the

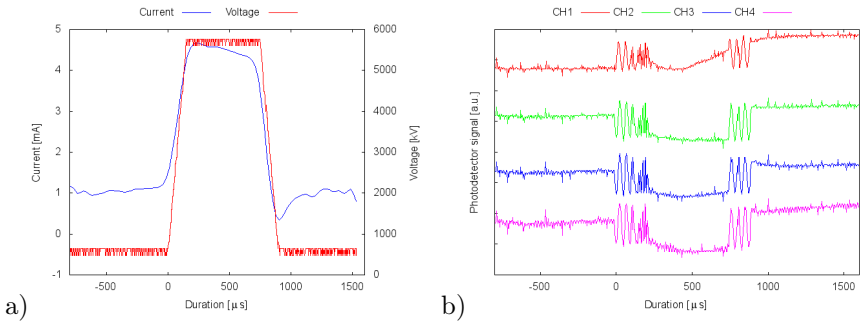

Figure 34: (a) Higher voltage pulse applied to finish KTP poling, (b) oscilloscope traces showing the end of poling process.

experiment we also tried to do KTP overpoling applying a few higher voltage

pulses (∼6–9 kV) after the poling process was done. In this case, more and more domains around the stripes in patterned electrode change the polarization and the duty cycle of the grating can be significantly affected. For the pulses of the voltage higher than 8 kV we observed even merging the domains at the periodic electrode side. It is evident, that the domain nucleation monitoring process plays the decisive role in the QPM devices production. All of the above is also true for KTA crystal, but the appropriate voltage of the pulse is higher (∼6.5 kV) due to the conductivity which is higher by almost one order of magnitude.

4.5.8 Etching the Ti electrodes

To remove the Ti electrodes for the further possibility of domain characterization chemical etching process was used. According to the [76] chemical etchtants act with different speed on the positive and negative domains and therefor help to reveal them. For etching we use a solution of $NH_4OH + H_2O_2 + H_2O$ in proportion to 1:1:4 at 60 °C. Firstly, H_2O is heated up to 80 °C in a glass tray, after that one part of H_2O_2 and one part of NH_4OH are added. All the substances should be quickly mixed. At last, the crystal covered with Ti electrodes is dipped into the etching solution. The etching time 1 minute 30 seconds is enough to remove a 100 nm thick Ti layer.

4.5.9 Characterization of the domains

To inspect and evolve the domain structure, Nomarski interference contrast microscopy and atomic force microscopy (AFM) [77] are probably the most exploitable techniques. To our experience, the Nomarski contrast microscopy is mainly suited for PPKTP crystal (Fig. 35), in the case of PPKTA crystal the contrast between domains is extremely weak and it is hard to measure the domain size.

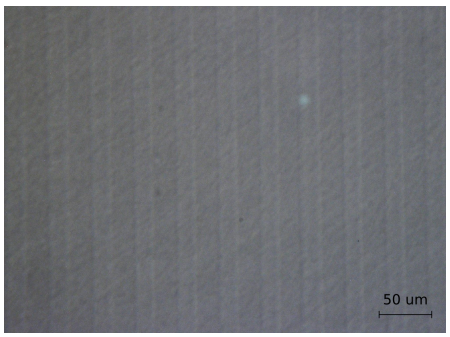

Figure 35: QPM graiting in PPKTP imaged with the Nomarski contrast microscope. Period is 35.9 μm.

AFM in a piezoresponse force microscopy (PFM) mode [78] is one of the reliable and more informative way to evaluate the domains structure in variety of ferroelectrics.

Side	Topographic image	Phase image
c^+	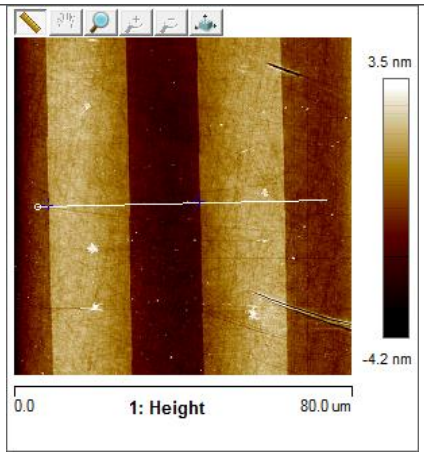	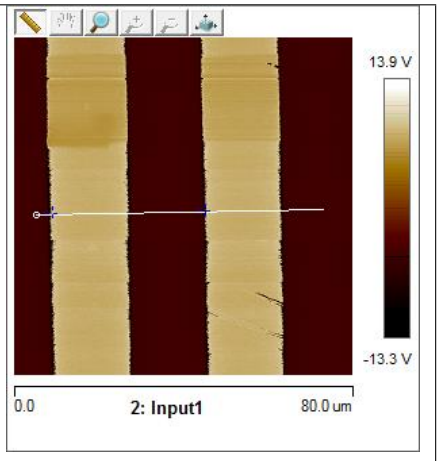
c^-	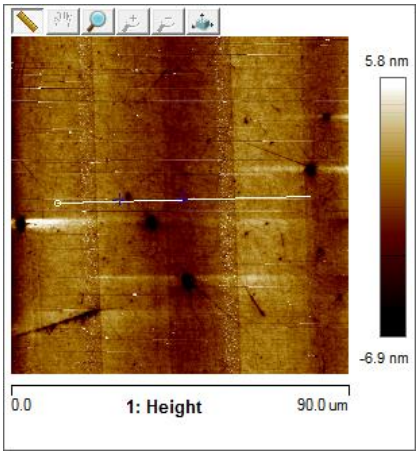	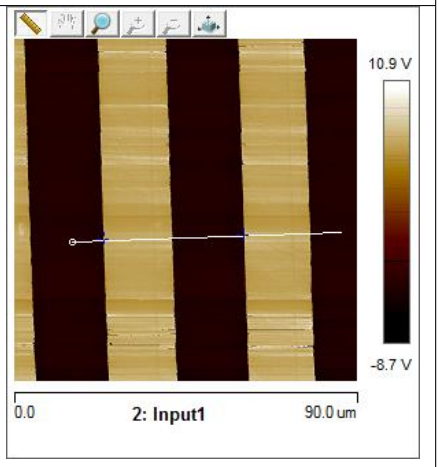

Figure 36: AFM images of height profile and piezo response phase of a good quality PPKTP.

Side	Topographic image	Phase image
c^+	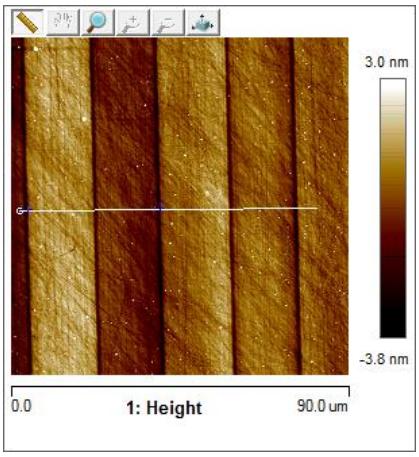	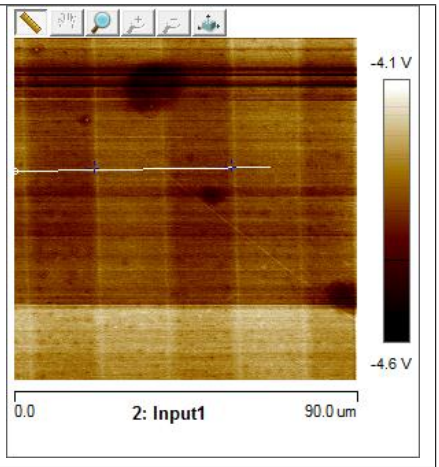
c^-	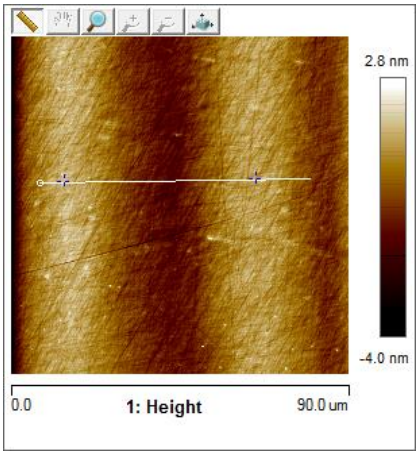	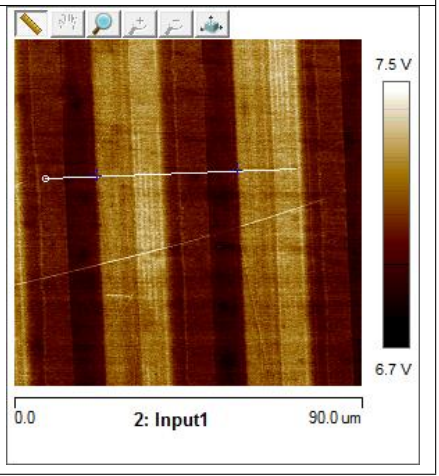

Figure 37: AFM images of height profile and piezo response phase of an overpoled KTP.

From the AFM images in Fig. 36 it is seen that the ∼3 nm difference in domains heights is measured on c^+ side of the crystal and almost no hight difference on c^- side. To measure the period of the QPM device the phase image is more suitable. The contrast between the two neighbor domains with the opposite nonlinear coefficient sign is legibly seen. The periodicity measured on both faces of the PPKTP poled in our laboratory is 35.87 μm what is very close to the photolithography mask period of 35.9 μm. An almost equal duty cycle of the grating is measured on both sides (∼50%).

The images obtained from the over poled KTP crystal also contains interesting features. It is hard to find any difference in a hight profile between this sample and good quality PPKTP, but the phase behavior is absolutely distinguishable. Domains on the c^+side have very week contrast, what is the evidence of the domain merging at this face. Contrary, on the c^-face at least four regions with various phases are visible. It means that the different number of domains reverted inside the crystal at each of these regions. The crystal now is inappropriate for DFG generation with the calculated period. But even this technique can be used to produce the QPM structures with the doubled period [79].

In case of obtaining bad quality periodical pattern inside the crystal the higher than coercive field voltage can be applied between two polar faces to orient all the domains along the applied electric field and produce single domain crystal again.

4.6 The DFG experiment with PPKTP and PPKTA

Experimental results described here were first presented by the author and his colleagues in [C5,C9,C10,C11] and published in [P1,C8].

The DFG experiments were performed for two types of periodically poled nonlinear crystals. KTP crystals with periods of 35.4, 35.6, 35.9, 36.1 μm and aperiodic structure described by function $\Lambda_{KTP}(x)$ (see section Methods), and KTA crystals with periods 39.8 and 40.1 μm and aperiodic structure described by function $\Lambda_{KTA}(x)$. Earlier, in part 4.2 we mentioned, that the simple tunable ring Yb- and Er-doped fiber lasers were chosen as a fundamental sources for our first prototype of the mid-IR sources based on the DFG. After the amplifiers, the linearly polarized light from the multiplexer PM-WDM output (see Fig. 38) is collimated by an anti-reflective coated (ARC) achromatic lens L1 (Thorlabs, PAFA-X-4-C) with an effective focal length of 4 mm and then focused into the center of the periodically poled crystal by means of an ARC achromatic doublet L2 (Thorlabs, AC254-030-C-ML) with a focal length of 30 mm, which is close to optimal (see Section 3.4). The used PPKTP and PPKTA crystals have a length of 16.5 mm and a thickness of 1 mm. The length of the periodically poled pattern is 15 mm. After passing the crystal, the beams go through a collimating calcium fluoride lens L3 (Thorlabs, LA5042). A dichroic filter F (Thorlabs, DMLP1800R) separates the propagated pump and signal radiation from the idler radiation. A concave lens L4 (Thorlabs, LD1357) is used to prevent damage to the control detector D1 (Thorlabs, PDA10A). A germanium window GW

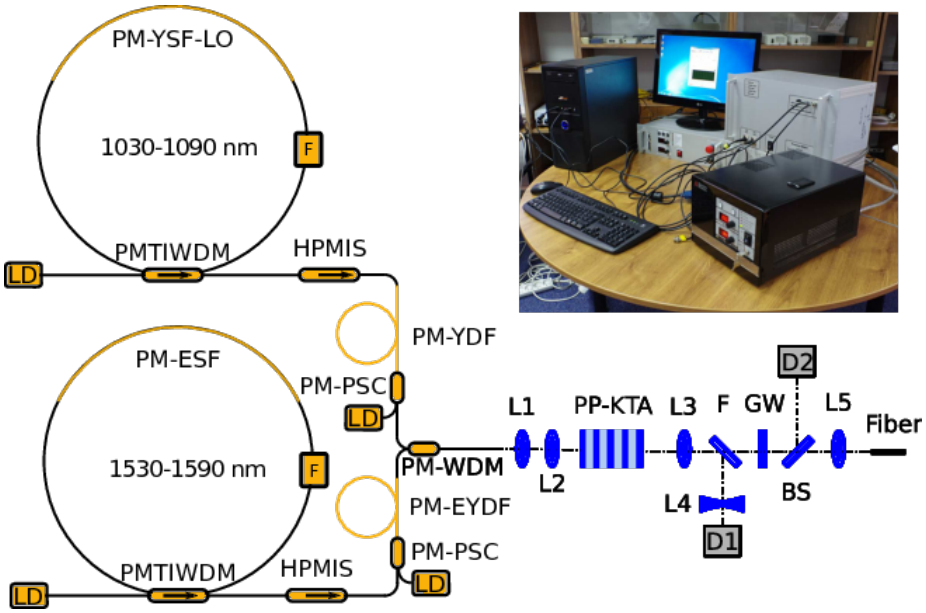

Figure 38: The DFG experiment. Inset: photo of mid-IR laser source prototype.

(Thorlabs, WG91050) additionally blocks wavelengths shorter than 1800 nm. A beam splitter BS (Thorlabs, BP145B4) divides the idler radiation into two beams. The first beam goes to the PbSe detector D2 (Thorlabs, PDA20H-EC) and is used as a reference, and the second one is directed to the output chalcogenide fiber by using a Si-Ge achromatic doublet (Thorlabs, AC254-050-E) L5 for further convenient delivery of mid-IR radiation.

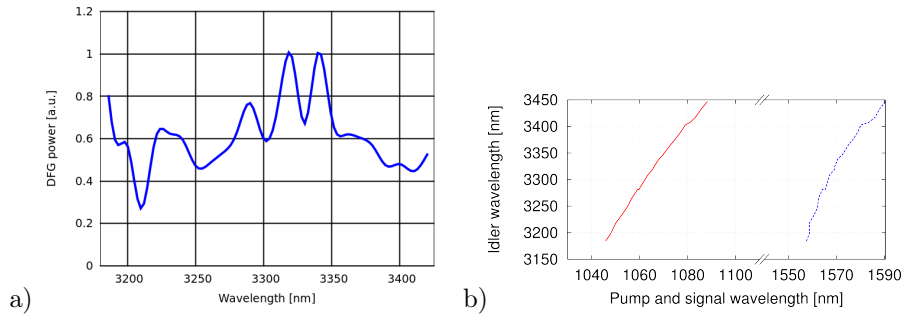

Figure 39: (a) DFG output power in PPKTP with the period of 35.9 μm within the (b) tuning ranges of the fundamental lasers.

In Figure 39(a) a behavior of DFG power in PPKTP with the period of 35.9 μm measured in the wide spectral range 3186–3420 nm at room temperature is presented. We attribute the oscillating behavior of the DFG power curve to the

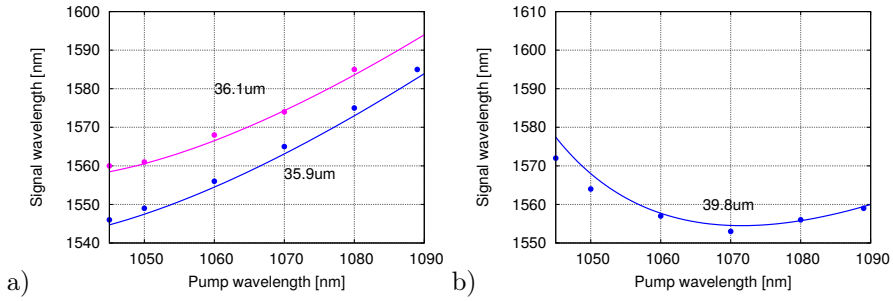

Figure 40: Theoretical (lines) and experimental (points) phase-matching conditions for (a) PPKTP crystal with periods of 35.9 and 36.1 μm, (b) PPKTA crystal with a period of 39.8 μm.

parasitic optical etalon effect and absorption of the water vapors in air. Figure 39(b) shows the dependence of the idler wavelength on the target wavelengths. The developed mid-IR source can be tuned in a broad range. For this, the fundamental lasers needed to be continuously tuned in order to maintain the phase synchronism and maximize the generated idler power as described in Section 3.4. The phase synchronism relations for PPKTP and PPKTA are shown in Figure40.

Next, we tried to compare the tunability performance of PPKTP and PPKTA in the same conditions. Figure 40 shows predicted by the theory and experimentally measured phasematching wavelengths for two gratings periods of 35.9 μm and 36.1 μm in PPKTP and one grating period of 39.8 μm in PPKTA crystals. The crystals with these periods demonstrated the broadest tunability. Interestingly, that in the PPKTP crystal the wavelengths of the ytterbium and erbium lasers should be tuned simultaneously in the same direction in order to maintain the phase synchronism. This co-directional changing of the fundamental frequencies leads to relatively small changes in their difference frequency. For the phase synchronism relations we also observed some deviations between the theoretical and measured results. The largest wavelength deviation of 0.32% was obtained for PPKTA crystal with the period of 39.8 μm at the pump wavelength of 1040 nm. This can be related to not an ideal prediction of the Sellmeier equation given by Fradkin-Kashi [26] and comparatively big tuning filter step $\sim$0.1 nm. In the experiment we achieved the maximum tunability over the mid-IR spectral range of 255 nm for the PPKTP crystal with pattern period of 35.9 μm (see Fig. 41). The shorter wavelengths can be achieved with a poling period of 36.1 μm at the expense of a narrower tuning range of 3165–3390 nm. The tuning law differs for the PPKTA crystal. We can see that the wavelength of the erbium-doped fiber laser should decrease over the extended range while the wavelength of the ytterbium-doped fiber laser grows. Because fundamental wavelengths change in the opposite directions over an extended spectral range, the KTA crystall allows to achieve a much larger change of the difference frequency with the same sources of the fundamental signals. The

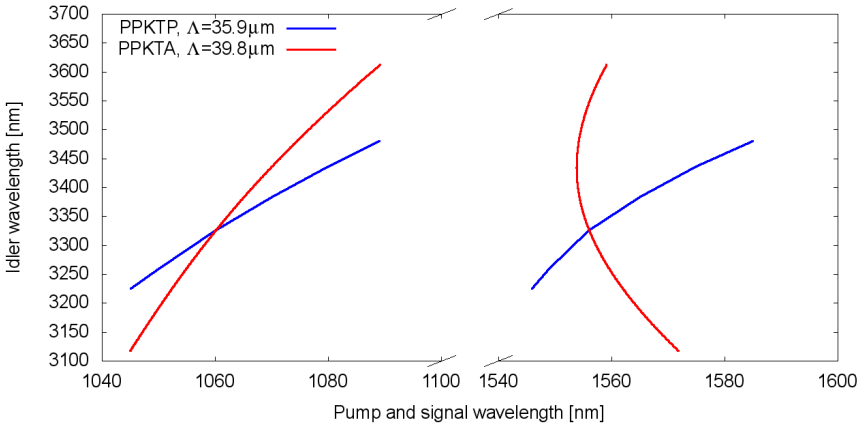

Figure 41: Tuning ranges for the PPKTP with a period of 35.9 μm (blue) and PPKTA with a period of 39.8 μm (red).

DFG generator based on a PPKTA crystal with a period of 39.8 μm covered the mid-IR spectral range of more than 520 nm. It is obvious that the mid-IR laser source based on PPKTA crystal can cover twice as high spectral range compared to the source based on PPKTP crystal for the same sources of the fundamental signals. Unfortunately, the crystal growth technology for the KTA crystal is not so mature as for the KTP crystal and almost three times higher price for KTA can limit its use.

4.7 DFG process optimization experiment

The results described in this section were presented by the author in [C7].

When the pump and signal beams are output overlapping from the WDM pigtail (see Fig. 38), the easiest way to focus them is utilizing one achromatic doublet for wide spectral range 1–1.6 μm. The advantage of this method is simplicity, but it also has a drawback like focal point shift for 1.06 μm and 1.55 μm ($\sim$ 250 μm, see Fig.4(b)). As was shown earlier in the theoretical part, the DFG process efficiency can be enhanced using optimal focusing conditions. For this, two fundamental beams need to be focused in the middle of the nonlinear medium with the signal beam being focused tighter than the pump beam. According to the numerical simulation (see Fig. 6), the highest output power is reached for $\omega_{0P} = 34\,\mu$m and $\omega_{0S} = 24\,\mu$m. For the single achromatic doublets it is hardly achievable because of the material dispersion. To prove the numerical simulation results, an experimental setup presented in Figure 42 was designed. In this setup the pump and signal beams can be focused separately. As a result, with different collimators (L1, L2) and different lenses (L3, L4) various waist sizes ω_{0P} and ω_{0S} can be reached for each fundamental beams.

In the inset of Figure 42 there is a simplified layout of the DFG source. It is based on a single-frequency widely tunable ytterbium-fiber laser TFL1060 de-

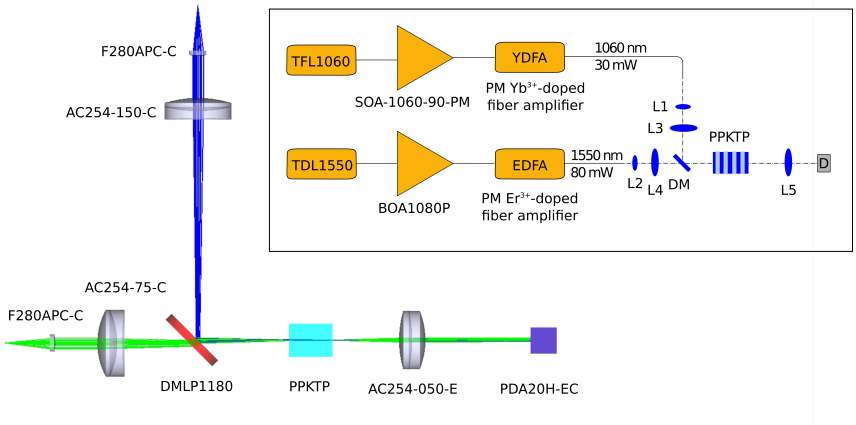

Figure 42: Experimental setup for different focusing conditions.

scribed earlier in Section4.3 and commercial tunable diode laser source TDL1550 (Agilent, 81600B) at 1.55 μm region. Their signals are amplified firstly in semiconductor optical amplifiers (SOA-1060-90-PM from INNOLUME and BOA1080P from THORLABS, respectively) to mW level and, secondly, in home-made fiber amplifiers YDFA and EDFA to tens of mW. Combining semiconductor and fiber optical amplifiers allows to suppress an amplified spontaneous emission at other wavelengths and achieve a spectrally flat gains. The z-axis polarized beams from the output pigtails are collimated by lenses L1 and L2 and then beams are focused into the center of the periodically-poled KTP crystal using achromatic doublets L3 and L4. The beams are combined using a dichroic mirror DM (Thorlabs, DMLP1180). The 3.3 μm difference frequency generation passes through a germanium lens L5 (Thorlabs, AC254-050-E), which also blocks the wavelengths shorter than 1.8μm, and goes to a PbSe-detector D (Thorlabs, PDA20H-EC).

In this setup the lenses L1, L2, L3 and L4 can be changed to other lenses to achieve the different waists sizes. The lenses L3 and L4 can be moved to change the waist position along the optical axis of the crystal. In the experiment we used two types of collimators from Thorlabs (PAFA-X-4-C and F280APC-C) and the achromatic doublets with nominal focal lengths of 30, 35, 40, 50, 60, 75 and 150 mm (Thorlabs, AC254 series). The highest output idler power was achieved for the collimators with the beam diameter of 3.4 mm (F280APC-C) and lenses with 150 mm focal length for 1060 nm arm and 75 mm focal length for 1550 nm arm. According to modeling in ZEMAX, these lenses provide the pump beam waist $\omega_{0P} = 29.5$ μm and the signal waist $\omega_{0S} = 21.7$ μm, which give $\xi_p \approx 1.6$ and $\xi_s \approx 4.3$. These values are the closest to the optimal calculated values ($\xi_p \approx 2$, $\xi_s \approx 5$ see Section 3.4) we can obtain for the available set of lenses. The measured idler powers for various sets of lenses were matched to the calculated values (see Fig.43). The other combination of lenses provided lower

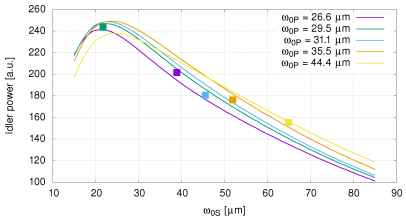

Figure 43: Idler power dependence on signal beam size ω_{0S} for various pump beam sizes ω_{0P} for PPKTP crystal with period of 35.9 μm. Lines are calculated values with FDM method, squares represent the experimental results. μm.

DFG power what was in good agreement with the model prediction.

The numerical simulation predicted relatively small, not higher than 5%, efficiency improvement of the DFG process. However, in practice it is difficult to fulfill ideally optimal focusing conditions and, moreover, there are always small errors in fill factor and periodicity during the poling process. As a result, the final efficiency enhancement can be even smaller than 1%. Adding here the mid-IR source instabilities of ±5% due to not ideally stabilized pumping diode current and temperature, parasitic optical etalon effects, and not thermally stabilized nonlinear crystal, it is hard to distinguish any efficiency enhancement within the measured data. We can conclude that using the complex two arms system is redundant for such a small improvement. In the final prototype of the spectroscopic mid-IR source we used a single achromatic doublet AC254-035-C for the fundamental beams focusing.

During all experiments the maximum achieved DFG output power ∼140 μW was obtained in KTA crystal with the aperiodic poling pattern $\Lambda_{KTA}(x)$ at 3320 nm for the pair of fundamental wavelengths of 1065 nm and 1568 nm. In many experiments the fundamental lasers run not at the same power levels, in this situation it is better to use a normalized conversion efficiency for the comparison of the results. The mentioned infrared power corresponds to the normalized conversion efficiency of 0.018 %/(W·cm). This value is almost two times higher than published earlier $\eta = 0.0091$ %/(W·cm) for the uniform period in [26]. Slightly lower efficiency (0.015 %/(W·cm)) was achieved for the period of 39.8 μm, and the lowest $\eta = 0.011$ %/(W·cm) for 40.1 μm. In the case of PPKTP, the highest idler power was 114 μW for the crystal with poling period of 35.9 μm, corresponding to the conversion efficiency of 0.012 %/(W·cm). The aperiodically poled KTP demonstrates the efficiency of $\eta = 0.01$ %/(W·cm). PPKTP with periods of 36.1 and 35.6 μm gave the lover output powers with the efficiency not exceeded $\eta = 0.01$ %/(W·cm), and significantly lower conversion efficiency of $\eta \sim 0.004$ %/(W·cm) was obtained for the period of 35.4 μm. The conversion efficiencies values for PPKTP are also in good agreement with the literature [25, 80]. For numerous spectroscopic applications mid-IR power level of tens of μW can be enough.

5 Application of mid-IR generator

In this chapter, the possible application of the developed widely tunable narrowband mid-IR source has been described. As it was mentioned in introduction part, our main motivation is usefulness of this device for the laser absorption spectrometry because many fields like medicine [81, 82], agriculture [1], environmental monitoring [83] and industry [84] take advantage of such a source. The operating wavelength range of the designed laser (∼3-3.8 um) falls in one of several infrared atmospheric windows with minimal interference from water vapors, CO_2, or the major constituents of air, nitrogen and oxygen. Many molecules with trace concentrations and potential interest for an atmosphere monitoring (CO, NO, N_2O, CH_4, H_2CO, NH_3, SO_2, etc.), a control of global warming induced by greenhouse gases (i.e., C_2H_2, OCS, HCl, C_2H_4, etc.), fluorocarbons, volatile organic compounds (VOCs), and aerosols have strong fundamental rotational-vibrational absorption bands in this spectral region (see Fig.44) [83] and, therefore, can be detected using the developed laser source. The narrow linewidth of the laser is mainly important for the small

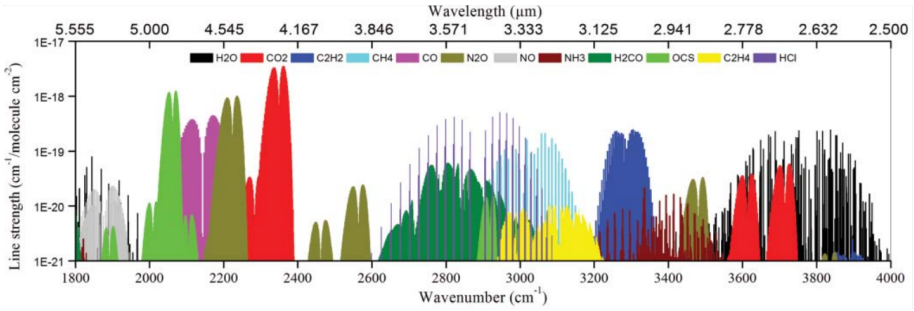

Figure 44: Absorption spectra for major atmospheric species simulated by HITRAN [85]. Reprinted from [83] with permissions from Taylor & Francis.

molecules with good resolved absorption lines, where it is possible to choose a strong absorption feature in a band free of interference from other gases and perform the measurement. The wide tunability of the laser is required for complex gas mixtures, large molecules with many atoms, or heavy atoms, because such analytes do not have good resolved absorption features or have congested rovibrational spectrum and need to be scanned far enough to certainly measure their wide or overlapped absorption bands. For example, toxic hydrocarbon gases (toluene, benzene, ethylbenzene, xylene etc.), which are important in an environmental sensing, have a number of CH stretching absorption lines in the region between 2800 and 3100 cm^{-1}(∼3570 – 3225 nm).

The laser source with the appropriate wavelength, power, linewidth and tunability together with an optimal detector are only a part of a good spectroscopic system. Such fundamental parameter of the system as detection sensitivity can be improved by using multi-pass cells filled with the gas sample, where the beam undergoes multiple reflections between two mirrors. Additionally,

reducing the gas pressure by evacuating the cell narrows the absorption lines. The narrowing of the absorption lines significantly improves another essential system parameter—selectivity. During the last decades various techniques were developed to enhance the performance of the laser absorption spectroscopy [C8].

5.1 Experiment with toluene

Results presented in this part of thesis were published by our team in [C8] and presented by the author at [C5].

Firstly, to test the developed mid-IR laser source, very simple direct absorption spectroscopy experiment with toluene ($C_6H_5CH_3$) was performed. Toluene was chosen as an illustrative easily accessible aromatic hydrocarbon with a single CH_3 group. The structure of the toluene is shown in Fig.45(a). Toluene has a number of CH stretching absorption lines in the working region of the designed mid-IR source. The CH stretches is observed at 2800 - 3100 cm^{-1} wavenumber region [86]. There is an IR absorption spectrum of toluene at room temperature diluted by N_2 at atmospheric pressure downloaded from HITRAN database [87] in the mentioned region in Fig.45(b). The aim of the experiment was the sensitivity test of the spectroscopic system by measuring the absorption of toluene with various concentrations at two fixed wavelengths.

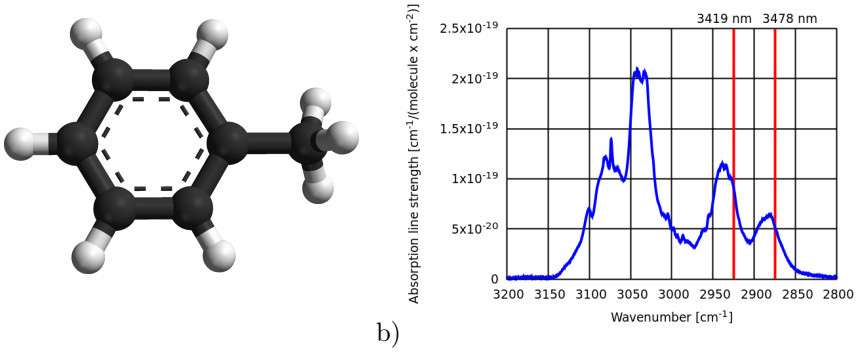

a) b)

Figure 45: (a) Toluene structure [88]. (b) IR absorption spectrum of toluene [87]. Vertical red lines depict the laser lines used in the experiment.

A schematic setup of the experiment is shown in Fig.46(a). The light from the developed narrow-band mid-IR source is collimated by a Si-Ge achromatic doublet (Thorlabs, AC254-050-E), this collimator additionally filters the residual pump and signal radiation after the nonlinear crystal. Then a pellicle beamsplitter (Thorlabs, CM1-BP145B4) splits the infrared light into a reflected reference beam and transmitted probe beam. The reference beam is detected by a PbSe reference detector (Thorlabs, PDA-20H). A mid-infrared enhanced protected gold mirror (Thorlabs, PF10-03-M02) directs the probe beam through a BaF_2 entrance window to an astigmatic multi-pass absorption cell (Aerodyne, AMAC-76) with a designed absorption path length of 76 m and volume of

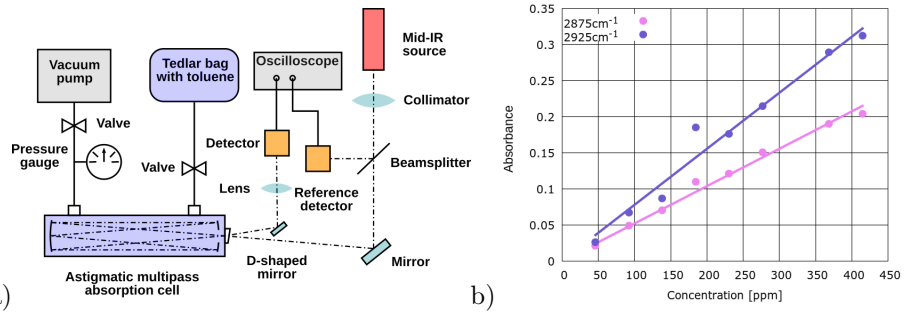

Figure 46: (a) Schematic diagram of the experimental setup. (b) Absorbance dependence on the toluene concentration at two different wavenumbers.

0.5 L. The working wavelength range of the cell is from 3 to 11 µm. After passing the absorption cell and reflection from a D-shaped mirror (Thorlabs, PFD05-03-M01), the light is focused by a CaF_2 lens of 75 mm effective focal length (CAPX12, Newport) onto a thermoelectrically cooled mercury-cadmium-telluride (MCT) IR detector module with a built-in preamplifier (HAMAMATSU, C12495-211S). Signals obtained from both of the detectors were measured by an oscilloscope (Rigol, DS 1052E).

Toluene has two wide absorption bands near the wavenumbers of 2875 cm^{-1} (∼3478 nm) and 2925 cm^{-1}(∼3419 nm) which suit well for the test of the sensitivity of the developed system. As these absorption peaks are broadband, the sensitivity of the system mainly depends on the pressure of the gas. Before the experiment, eight Tedlar bags of capacity of 5000 mL were filled with a filtered air provided by a pure air circulator unit (Thorlabs, PACU™) without particulates, moisture, and VOCs. Then toluene/pure air mixtures of various concentrations were prepared by injecting of some amount of toluene in these bags. Below we describe how to calculate the necessary amount of toluene to prepare the gas mixture with known concentration. Concentration of the toluene in parts-per-million units (ppm, 10^{-6}) can be found from the equation

$$C_{ppm} = \frac{10^6 V_t}{V_t + V_d} \approx \frac{10^6 V_t}{V_d},$$

where V_t is toluene volume and V_d dilutant volume (5000 mL). From this equation the volume of toluene is

$$V_t = V_d C_{ppm} 10^{-6}.$$

The toluene volume at a room temperature of 25 °C and pressure of 100 kPa can be also expressed from the ideal gas low as

$$V_t = \frac{m}{M}\frac{RT}{p},$$

where m is mass of toluene, M is molar mass of toluene, p is gas pressure, R is ideal gas constant and T is temperature. From these two equations we can find the mass of the liquid toluene that should be evaporated in the Tedlar bag as

$$m = \frac{MV_d C_{ppm} 10^{-6}}{\frac{RT}{p}}. \tag{18}$$

Now, knowing the density of the toluene ($\rho = 0.867 g/cm^3$), we can calculate its volume as $V_t = m/\rho$. For example, 9 μL of toluene should be injected into 5 L Tedlar bag in order to achieve the concentration of 415 ppm. Eight gas mixtures with the concentrations from 45 to 415 ppm prepared in this way were measured during the experiment.

The multi-pass absorption cell was evacuated by a mini diaphragm vacuum pump with a fine control valve and a vacuum gauge (KNF LAB, N 816.3 KN.45.18). A perfluoroalkoxy (PFA) tubing, which has a high chemical resistance, was used to connect the pump and the bag with a sample to the cell. First, the cell was evacuated to the pressure level of 90 kPa. Then the signals at the laser working wavelength of 3419 nm (2875 cm^{-1}) were taken with the signal and reference IR detectors. After that, the cell was filled with the prepared air-toluene gas mixture, evacuated again to the pressure of 90 kPa, and transmitted through the cell laser signal and reference signal were measured again. The same measurements were performed for all prepared air-toluene gas mixtures. These measurements were repeated for the second absorption band at 3478 nm (2925 cm^{-1}).

After the measurements we were able to calculate the fraction of the laser light which is transmitted through the air-toluene gas sample, i.e. transmittance, as

$$T = \frac{S_t/R_t}{S_v/R_v},$$

where S and R are signals measured at the signal and reference detectors, respectively, and t and v are referred to the cell filled with toluene and without toluene. In conventional absorption spectrometry the absorbance value is used more often. The absorbance shows the attenuation of the light by the the gas sample and it is equal to the natural logarithm of the reciprocal transmittance:

$$A = \ln(\frac{1}{T}). \tag{19}$$

Using this approach we could calculate the absorbance of toluene for various concentrations (depicted in Fig.46(b) with dots). On the other hand, according to the Beer-Lambert law, the absorbance has a linear dependence on the concentration c of the analyte [89]:

$$A = aLc,$$

where a is an absorptivity factor and L is the effective path length of the light interacting with the gas sample. As can be seen from the Fig.46(b), measured

values of absorbance are well fitted with the liner model for the both of the absorption peaks of toluene.

In this experiment the best sensitivity for these two relatively weak peaks of toluene assumed to be at the level of ∼10 ppm.

5.2 Experiment with BANARG

The second spectroscopy experiment was decided to perform with such an indispensable gas as ethylene C_2H_4 since it is widely used in the chemical industry for polyethylene and plastic production. Ethylene is also an important gaseous phytohormone [90] which is used for stimulating of bananas and citrus fruit growth and ripening, degreening tomatoes and preventing onions and potatoes from germinating. In addition, ethylene as an specific air pollution in an urban environment can cause a stress for plant growth and development [91] even though ethylene pollution is not considered as a pollutant that has any effects on the global environment. In a medicine field, during inflammation ethylene is produced and quickly released in exhaled breath as a biomarker of bacterial infection [82]. In all these processes trace concentrations of ethylene can be detected with the laser spectroscopy.

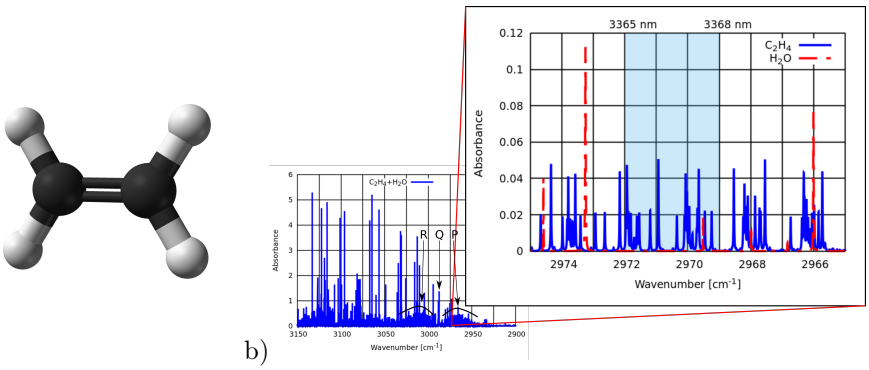

a) b)

Figure 47: (a) Ethylene structure [92]. (b) IR absorption spectra of ethylene and water [87]. Shaded blue area corresponds to the laser tuning range in the experiment.

The structure of the ethylene molecule is shown in Fig.47(a). In our experiment we used BANARG gas. It is a gas mixture designed to be used in greenhouses and consists of 96% of nitrogen N_2 and 4% of ethylene C_2H_4. In Fig.47(b) there is an absorption spectrum of ethylene together with the spectrum of water downloaded from HITRAN database [87] in a region of 3150–2900 cm^{-1}. This ro-vibrational line spectrum includes of P- (vibrational transitions with the rotational quantum number $\Delta J = -1$), Q- ($\Delta J = 0$), and R- ($\Delta J = 1$) branches, which consist of a lot of narrow lines. Moreover, ethylene lines overlaps with the lines of water in this region. In the inset we showed a more detailed absorption spectrum of ethylene to unveil the fine lines structure in P-branch. Also, in the inset, the water absorption spectrum depicted separately for clarity.

The aim of the experiment was a demonstration of the possibility to use our laser source for the mid-infrared panoramic molecular absorption spectroscopy. It means measure not only a few absorption lines, as most of spectroscopy systems do, but perform the measurements in different spectral regions. For example, when in one region the absorption lines of the interested molecule are influenced by the water lines, we can take more qualitative measurement in another region, where the water influence is minimal. The working wavelength range of the developed infrared laser can cover all lines in P-, Q-, and R-branches in the ethylene molecule. For our experiment we chose two different regions. One measurement was done within the P-branch, and the second measurement was taken within the Q-branch, where the lines are the most strong.

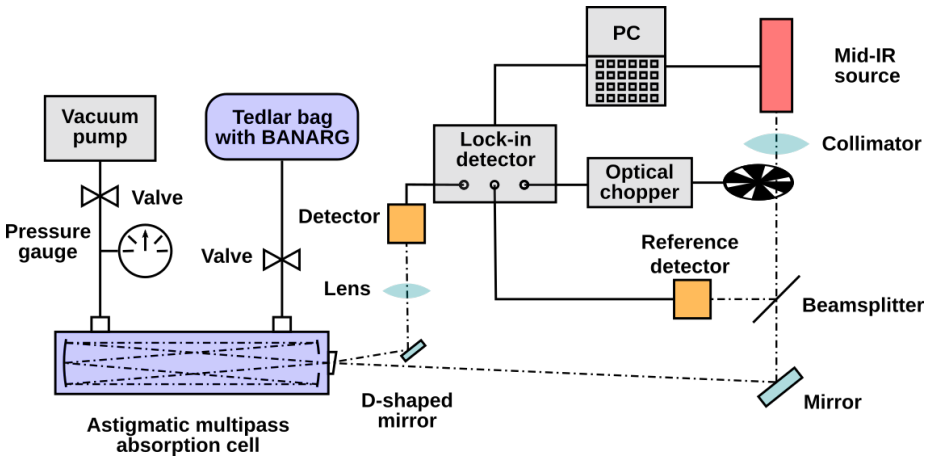

Figure 48: Experimental setup for ethylene measurement.

The setup presented in Figure 48 was used for the spectroscopic experiment with BANARG. For the study of ethylene, seven C_2H_4/N_2 mixtures with C_2H_4 concentrations of 800, 400, 240, 160, 80, 40 and 8 ppm were prepared. For this, the 5-liter Tedlar bags were filled with pure nitrogen and then BANARG was added to each bag. The appropriate amount of BANARG was calculated according to eq.18. A measurement procedure for each wavelength within the tested ranges was the same as described in subsection 5. Firstly, the laser was tuned within the P-branch from 2972 cm^{-1} (3365 nm) to 2969 cm^{-1} (3368 nm) (depicted as a blue shaded area in Fig.47(b)) with a step of 0.01 nm. There are a few easily distinguishable absorption peaks of ethylene and low interference with the omnipresent water peaks in this region. Then, the laser was tuned within the Q-branch from 2989 cm^{-1} (3345.6 nm) to 2986 cm^{-1} (3349 nm). There is also a strong water peak at 2987.5 cm^{-1}near the ethylene peak at 2988.3 cm^{-1}.

During the measurements, the level of a background signal at both detectors was $\sim$2 V. At such a high background signal level it is difficult to measure small signal changes caused by the absorption of low concentrated gas. Besides that, every measurement system suffers from the noises, signal offset and drift.

To improve the sensitivity of the detection system (to increase the signal-to-noise ratio of the data) we decided to modulate the output laser signal with an optical chopper (Thorlabs, MC2000B-EC with MC1F15 blade) at a frequency of 1000 Hz and employ a lock-in detection method [93]. For this method, we took the periodic signal from the chopper, as a reference, and the noisy measured signal, and used a phase-sensitive detection (PSD) technique to extract only that part of the measured signal whose frequency and phase match the reference signal. In our experiment lock-in detection was performed in software. The data from the detectors and modulator were acquired using three analog input channels of a data acquisition (DAQ) card (National Instruments, PCI-6229) and a LabVIEW program was developed for the data analysis. The measured data were processed in the same manner as was described in the previous section.

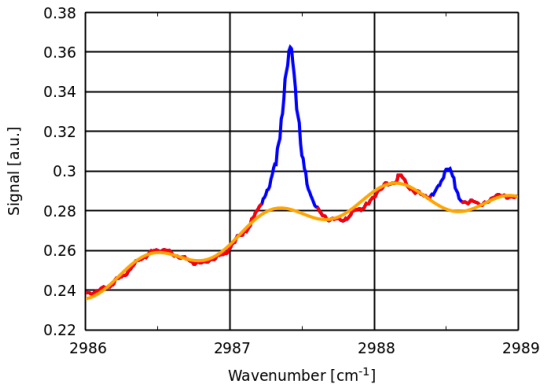

Figure 49: Measured reference signal for the empty gas cell. The instrumental influence is highlighted in orange.

In this experiment with the wavelength scanning we discovered one more issue to solve. In Fig.49 there is an example of measured signal in 2986–2989 cm^{-1} range. There is the reference signal for the gas cell without the ethylene sample. Here we see not only two water absorption peaks (blue), but also some background signal with oscillating behavior (red). The oscillating background can be fitted by sum of two different sine functions (orange). We attribute this oscillations to parasitic optical etalon fringes [94] produced by the light interference between some surfaces in the optical path. This instrumental influence can be eliminated from the absorbance calculation (see eq.19) dividing the measured signal by this background function. The measured absorbance of the ethylene obtained in this way is presented in Fig.50.

In the right inset of Fig.50 there is an example of the measured absorbance (red) of ethylene with the concentration of 800 ppm within the P-branch. For the comparison the data provided by HITRAN database for ethylene (blue) of the same concentration in a gas-cell with the length of 9 m are also presented. It is seen that the measured data corresponded well with existing data in the

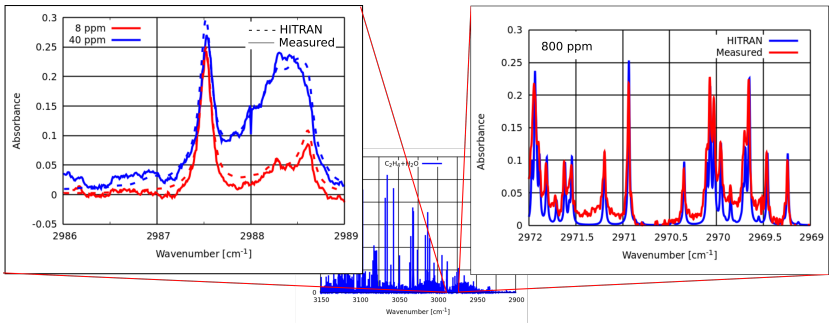

Figure 50: Measured absorbance of ethylene compared to data provided by HITRAN database.

database. The detection limit of the system reached in the experiment at this part of spectrum was ∼160 ppm. Such low reached sensitivity was connected to the weak absorption of the P-branch spectral lines. For the Q-branch near the region of 2988.3 cm^{-1}, where the absorption lines of the ethylene are more intensive, the sensitivity of our system was much better (see the left inset of Fig.50). We were able to detect the ethylene with the concentration of ∼8 ppm.

In both absorption spectroscopy experiments with the developed mid-IR narrow-linewidth laser only moderate sensitivity levels (∼ppm) were achieved. The reason is a non-optimal spectroscopic part of the setup. As the last measurement with ethylene revealed, the real path length inside the multipass cell was about 9 m long only. For the ideal alignment of the cell with a path length of 76 m we expect an improvement of sensitivity of more than one order of magnitude. Eliminating the parasitic optical etalon fringes, that we observed in all measurements, is another way of enhancement. Using a hardware with higher input resolution, e.g., 18 bit, more advanced software, and, especially, alternative to lock-in detection technique wavelength modulation spectroscopy (WMS) also has a great potential for sensitivity improvement. For the optimized spectroscopy system we expect the sensitivity at ppb – sub-ppb level, which is common for contemporary devices [81, 83]. But even obtained preliminary results in the application experiments clearly demonstrate the usefulness of the developed widely tunable narrowband mid-infrared source for the laser spectroscopy.

Conclusions

The main subject of the dissertation was an experimental investigation of the periodically poled nonlinear crystals for difference frequency generation of fiber lasers. The fiber lasers were based on Yb- and Er-doped active fibers worked in the 1.06 and 1.55 μm wavelengths bands, respectively. Narrow linewidths and wide tunability of the lasers permitted to use them as fundamental sources for difference frequency generation in periodically poled KTP and KTA crystals in a mid-infrared range of 3.1–3.6 μm. Such a broad working range allowed to build a prototype of MIR laser source suitable for high-resolution panoramic absorption spectroscopy. Preliminary results of the spectroscopic experiments with toluene and ethylene were presented. Additionally, the poling process of the nonlinear KTP and KTA crystals was reestablished at our lab. Numerical modeling of the optimization of the DFG process was also described.

In the first chapter an overview of the most popular mid-infrared laser sources used in recent years as well as the possibility to use them for the laser absorption spectroscopy of trace gases were presented.

In the second chapter the main aims of the dissertation were defined.

In chapter 3 the used methods were described. In the beginning, a brief theoretical introduction to a parametric nonlinear interaction was done. Then, a description of the advantages of quasi-phase-matching technique compared with birefringent phase-matching was followed by the reasons for choosing KTP and KTA crystals for a down-conversion of optical frequency. The second half of the chapter was dedicated to numerical modeling of the DFG process for the focused Gaussian fundamental beams. This numerical simulation was done using the author's MATLAB code based on finite element method. From the model the optimal poling periods of 35.8 μm for PPKTP and 40.0 μm for PPKTA for 1060 nm pump and 1550 nm signal wavelengths were calculated. The $\sim$5% conversion efficiency enhancement of the nonlinear process was predicted by simulation for the non-equal optimal focusing conditions for the pump beam $\xi_p \approx 2$ and tighter focused signal beam $\xi_s \approx 5$. The Gouy phase shift compensation with a further $\sim$1% efficiency enhancement with introduced aperiodicity in the poling pattern was also confirmed by the numerical modeling employing the Fourier transform beam propagation method. This simulation of the aperiodic structure was done earlier by the author's colleagues and reiterated by the author using his code based on the finite element method. Both methods gave qualitatively similar results across the same conditions.

Chapter 4 represented the experimental part of the dissertation. In the first section Yb-doped high-power fiber laser in a linear configuration was compared to ring Er-doped fiber laser in a master oscillator power amplifier configuration. The tunability of both lasers was almost equal ($\sim$50 nm), on the other hand, the stability and reliability at a few watts output power level for the ring Er fiber laser with MOPA configuration was much better. The laser linewidth of the ring resonator also was much narrower ($\sim$2.4 GHz) then for the linear resonator.

Subsequent work was primarily devoted to the laser line narrowing in the ring fiber resonators. Simple fiber ring configuration with a narrowband tunable filter

provided the linewidth of $\sim$ 600 MHz in CW regime with the wide tunability of $\sim$ 70 nm. The setups with a double-pass filter and tracking filter further narrowed the linewidth up to $\sim$ 100 MHz, but additional components in the resonator, especially circulator, significantly decreased the tunability and output power. Compound fiber resonator had the minimum linewidth of $\sim$ 75 MHz, almost the same tunability as the ring configuration, but lower power and tendency to damage an amplifier stage. As a compromise between the narrow linewidth, high tunability, sufficient output power, and reliability, the simple ring configuration was chosen for the first prototype of mid-IR source. The next developed laser configuration was a single-frequency ytterbium-doped fiber laser based on a fiber ring resonator filter. Active stabilization of the resonator length resulted in the laser linewidth of $\sim$11.7 kHz and broad tunability from 1023 nm to 1107 nm without the mode-hopping. This single longitudinal mode laser together with a commercial widely mode-hop free tunable diode laser at the wavelength of 1.55 μm with the linewidth of 100 kHz was used in the final prototype of the spectroscopic mid-IR laser source.

The next section of the chapter described the creation of high power Yb- and Er/Yb-doped fiber amplifier. The radiation of the developed fiber lasers was amplified to the Watt-level of output power.

After that, all steps of the periodically poled KTP and KTA crystals fabrication using low-temperature electric field poling technique were described in detail. These included a periodical pattern formation using a photolithograpy process based on the positive resist Shipley Microposit S1818G2 and Ti electrodes vacuum deposition. Under the applied field the polarity of the ferroelectric domains was changed to the opposite. Experimentally was found, that 3-4 pulses of a voltage of $\sim$ 5.5 kV was enough for the fabrication of good quality periodical structure inside KTP crystal, and $\sim$ 6.5 kV for KTA crystal. Monitoring methods with the current control and the transverse electro-optic effect in the crystal were implemented. The characterization of the domains was done using Nomarski contrast microscope and atomic force microscopy in a piezoresponse force microscopy mode.

Next, generation of the difference frequency of the developed narrowband tunable fiber lasers in periodically poled KTP and KTA crystals was performed. The maximum tunability over the mid-IR spectral range of 255 nm was achieved for the PPKTP crystal with a pattern period of 35.9 μm. For the PPKTA crystal with a period of 39.8 μm the covered mid-IR spectral range was more than 500 nm. The highest MIR power of $\sim$140 μW was obtained for aperiodically poled KTA and corresponded to the normalized conversion efficiency of 0.018 %/(W$\cdot$cm). In the end, the results of numerical simulation provided optimal focusing conditions were successfully verified during the experiment with the possibility to change focusing lenses.

In chapter 5 potential application of the developed DFG mid-IR source based on high-power fiber lasers for high-resolution absorption spectroscopy was presented. Preliminary results in the experiment with an astigmatic multi-pass absorption cell filled with toluene indicated a sensitivity at the level of $\sim$10 ppm. The second experiment with ethylene employed a lock-in detection method and

demonstrated the system detection limit better than 160 ppm.

The most important contributions of the dissertation:

- Design of the numerical code in MATLAB for DFG process modeling and optimization using FEM.
- Systematization and comparison of approaches to laser line narrowing for the ring fiber lasers.
- Comparison PPKTP with its isomorph PPKTA from point of better tunability in mid-IR.
- Recommencement, disclosure, and detailed description of the low-temperature electric field poling technique for fabrication of periodically poled KTP and KTA crystals.

In summary, all goals defined in chapter 2 were successfully achieved.

References

[1] S. M. Cristescu, S. T. Persijn, S. Te Lintel Hekkert, and F. J M Harren. Laser-based systems for trace gas detection in life sciences. *Applied Physics B: Lasers and Optics*, 92(3 SPECIAL ISSUE):343–349, 2008.

[2] Chuji Wang and Peeyush Sahay. Breath analysis using laser spectroscopic techniques: Breath biomarkers, spectral fingerprints, and detection limits. *Sensors*, 9(10):8230–8262, January 2009.

[3] Chayan Mitra. Mid-Infrared Spectroscopy and Challenges in Industrial Environment. In *Infrared Spectroscopy - Principles, Advances, and Applications*. IntechOpen, March 2018.

[4] S. Hugger, F. Fuchs, J. Jarvis, M. Kinzer, Q. K. Yang, R. Driad, R. Aidam, and J. Wagner. Broadband-tunable external-cavity quantum cascade lasers for the spectroscopic detection of hazardous substances. page 86312I, February 2013.

[5] R. F. Curl and F. K. Tittel. Tunable infrared laser spectroscopy. *Annu. Rep. Prog. Chem., Sect. C: Phys. Chem.*, 98(7):219–272, 2002.

[6] Jane Hodgkinson and Ralph P Tatam. Optical gas sensing: a review. *Measurement Science and Technology*, 24(1):012004, November 2012.

[7] Frank K Tittel, Rafal Lewicki, and Robert Lascola. Emerging Infrared Laser Absorption Spectroscopic Techniques for Gas Analysis. *Laser Absorption Spectroscopic Techniques*, pages 71–110, 2013.

[8] A. Kosterev, G. Wysocki, Y. Bakhirkin, S. So, R. Lewicki, M. Fraser, F. Tittel, and R. F. Curl. Application of quantum cascade lasers to trace gas analysis. *Applied Physics B: Lasers and Optics*, 90(2):165–176, 2008.

[9] Sergey B. Mirov, Vladimir V. Fedorov, Dmitry Martyshkin, Igor S. Moskalev, Mike Mirov, and Sergey Vasilyev. Progress in Mid-IR Lasers Based on Cr and Fe-Doped II-VI Chalcogenides. *IEEE Journal of Selected Topics in Quantum Electronics*, 21(1):292–310, 2015.

[10] Darren D. Hudson, Alexander Fuerbach, and Stuart D. Jackson. *Progress in Mid-infrared Fiber Source Development*. 2019.

[11] Stuart D. Jackson. Towards high-power mid-infrared emission from a fibre laser. *Nature Photonics*, 6(7):423–431, 2012.

[12] Matthew R. Majewski and Stuart D. Jackson. Tunable dysprosium laser. *Optics Letters*, 2016.

[13] Ori Henderson-Sapir, Stuart D. Jackson, and David J. Ottaway. Versatile and widely tunable mid-infrared erbium doped ZBLAN fiber laser. *Optics Letters*, 2016.

[14] Maurus Tacke. Lead-salt lasers. *Philosophical Transactions of the Royal Society of London. Series A: Mathematical, Physical and Engineering Sciences*, 359(1780):547–566, March 2001.

[15] F. K. Tittel, R. F. Curl, L. Dong, J. H. Doty, A. A. Kosterev, R. Lewicki, D. Thomazy, and G. Wysocki. Recent Advances in Infrared Semiconductor Laser based Chemical Sensing Technologies. In *NATO Security through Science Series B: Physics and Biophysics*, pages 165–173. 2011.

[16] Frank K. TITTEL, Yury BAKHIRKIN, Anatoliy A. KOSTEREV, and Gerard WYSOCKI. Recent Advances in Trace Gas Detection Using Quantum and Interband Cascade Lasers. *The Review of Laser Engineering*, 34(4):275–282, 2006.

[17] Manijeh Razeghi, Wenjia Zhou, Steven Slivken, Quan-Yong Lu, Donghai Wu, and Ryan McClintock. Recent progress of quantum cascade laser research from 3 to 12 μm at the Center for Quantum Devices [Invited]. *Applied Optics*, 56(31):H30, 2017.

[18] Alfredo Bismuto, Stephane Blaser, Romain Terazzi, Tobias Gresch, and Antoine Muller. High performance, low dissipation quantum cascade lasers across the mid-IR range. *Opt. Express*, 23(5):5477–5484, March 2015.

[19] I Vurgaftman, R Weih, M Kamp, J R Meyer, C L Canedy, C S Kim, M Kim, W W Bewley, C D Merritt, J Abell, and S Höfling. Interband cascade lasers. *Journal of Physics D: Applied Physics*, 48(12):123001, April 2015.

[20] Caroline Amiot, Antti Aalto, Piotr Ryczkowski, Juha Toivonen, and Goëry Genty. Cavity enhanced absorption spectroscopy in the mid-infrared using a supercontinuum source. *Applied Physics Letters*, 111(6):061103, August 2017.

[21] Ian Coddington, Nathan Newbury, and William Swann. Dual-comb spectroscopy. *Optica*, 2016.

[22] J. Peltola, M. Vainio, V. Ulvila, M. Siltanen, M. Metsala, and L. Halonen. Off-axis re-entrant cavity ring-down spectroscopy with a mid-infrared continuous-wave optical parametric oscillator. *Applied Physics B: Lasers and Optics*, 107(3):839–847, 2012.

[23] M. Vainio and L. Halonen. Mid-infrared optical parametric oscillators and frequency combs for molecular spectroscopy. *Physical Chemistry Chemical Physics*, 18(6):4266–4294, December 2016.

[24] K. Krzempek, G. Dudzik, A. Hudzikowski, A. Gluszek, and K. Abramski. Highly-efficient fully-fiberized mid-infrared differential frequency generation source and its application to laser spectroscopy. *Opto-Electronics Review*, 25(4):269–274, December 2017.

[25] K Fradkin, A Arie, A Skliar, and G Rosenman. periodically poled KTiOPO 4. *Applied Physics Letters*, 74(7):914–916, 1999.

[26] K Fradkin-Kashi, A Arie, P Urenski, and G Rosenman. Mid-infrared difference-frequency generation in periodically poled KTiOAsO4 and application to gas sensing. *Optics letters*, 25(10):743–5, 2000.

[27] Peter Zeil, Nicky Thilmann, Valdas Pasiskevicius, and Fredrik Laurell. High-power, single-frequency, continuous-wave optical parametric oscillator employing a variable reflectivity volume Bragg grating. *Optics Express*, 22(24):29907, December 2014.

[28] D. J. Richardson, J. Nilsson, and W. A. Clarkson. High power fiber lasers: current status and future perspectives [Invited]. *Journal of the Optical Society of America B*, 27(11):B63, 2010.

[29] Michalis N. Zervas and Christophe A. Codemard. High Power Fiber Lasers: A Review. *IEEE Journal of Selected Topics in Quantum Electronics*, 20(5):219–241, 2014.

[30] Robert W. Boyd. Nonlinear Optics. *Book*, page 613, 2008.

[31] Richard L. Sutherland. *Handbook of Nonlinear Optics*, volume 36. 1997.

[32] J. A. Armstrong, N. Bloembergen, J. Ducuing, and P. S. Pershan. Interactions between light waves in a nonlinear dielectric. *Physical Review*, 127(6):1918–1939, 1962.

[33] L. E. Myers, R. C. Eckardt, M. M. Fejer, R. L. Byer, W. R. Bosenberg, and J. W. Pierce. Quasi-phase-matched optical parametric oscillators in bulk periodically poled LiNbO_3. *Journal of the Optical Society of America B*, 12(11):2102, 1995.

[34] Nonlinear crystals | optical crystals - eksma optics. `https://eksmaoptics.com/nonlinear-and-laser-crystals/nonlinear-crystals/`. Accessed on 08-04-2019.

[35] Ktp crystech inc. `http://www.crystech.com/product/23.html`. Accessed: 10-11-2019.

[36] John D. Bierlein and Herman Vanherzeele. Potassium titanyl phosphate: properties and new applications. *Journal of the Optical Society of America B*, 6(4):622, 1989.

[37] Kta crystech inc. `http://www.crystech.com/product/25.html`. Accessed 15-01-2019.

[38] S. C. Mayo, P A Thomas, S J Teat, G. M. Loiacono, and D N Loiacono. Structure and non-linear optical properties of KTiOAsO 4. *Acta Crystallographica Section B Structural Science*, 50(6):655–662, 1994.

[39] Covesion ltd. - material properties of lithium niobate. `https://www.covesion.com/support/covesion-guide-to-ppln/material-properties-of-lithium-niobate.html`. Accessed on 08-04-2019.

[40] David N. Nikogosyan. *Nonlinear Optical Crystals: A Complete Survey*. Springer-Verlag, New York, 2005.

[41] D. B. Kolker, O. L. Antipov, S. V. Larin, L. I. Isaenko, V. N. Vedenyapin, A. R. Ahmatkhanov, and V. Ya Shur. Mid-IR Optical Parametric Oscillator Based on Periodically Polled LiNbO3 Pumped by Tm3+:Lu2O3 Ceramic Laser. *Atmospheric and Oceanic Optics*, 32(6):724–729, 2019.

[42] O. Gayer, Z. Sacks, E. Galun, and A. Arie. Temperature and wavelength dependent refractive index equations for MgO-doped congruent and stoichiometric LiNbO3. *Applied Physics B: Lasers and Optics*, 91(2):343–348, 2008.

[43] G D Boyd and D A Kleinman. Parametric interation of focused Gaussian light beams. *Journal of Applied Physics*, 39(8), 1968.

[44] Tran-Ba-Chu and M Broyer. Intracavity cw difference frequency generation by mixing three photons and using Gaussian laser beams. *Journal de Physique*, 46:523–533, 1985.

[45] M. Broyer. Intracavity single resonance optical parametric oscillator (I.S.R.O.). *Journal de Physique*, 45(10):1599–1606, 1984.

[46] S. Stry, P. Hering, and M. Murtz. Portable difference-frequency laser-based cavity leak-out spectrometer for trace-gas analysis. *Applied Physics B: Lasers and Optics*, 75(2-3):297–303, 2002.

[47] S. Borri, P. Cancio, P. De Natale, G. Giusfredi, D. Mazzotti, and F. Tamassia. Power-boosted difference-frequency source for high-resolution infrared spectroscopy. *Applied Physics B: Lasers and Optics*, 76(4):473–477, 2003.

[48] D. Richter and P. Weibring. Ultra-high precision mid-IR spectrometer I: Design and analysis of an optical fiber pumped difference-frequency generation source. *Applied Physics B: Lasers and Optics*, 82(3):479–486, 2006.

[49] Inc. The MathWorks. *Partial Differential Equation Toolbox ™*. Natick, Massachusetts, United State, 2016.

[50] Shekhar Guha, Fei Jain Wu, and Joel Falk. The Effects of Focusing on Parametric Oscillation. *IEEE Journal of Quantum Electronics*, 18(5):907–912, 1982.

[51] S Guha. Focusing dependence of the efficiency of a singly resonant optical parametric oscillator. *Applied Physics B*, 66(6):663–675, 1998.

[52] Wei Xie, Xianfeng Chen, Yuping Chen, and Yuxing Xia. All-optical variable-in variable-out wavelength converter based on cascaded nonlinearity in aperiodic optical superlattice. *Optics Communications*, 251(1-3):179–185, July 2005.

[53] Feng Ji, Rongsheng Lu, Baosheng Li, Baigang Zhang, and Jianquan Yao. Mid-infrared tunable dual-wavelength generation based on a quasi-phase-matched optical parametric oscillator. *Optics Communications*, 282(1):126–128, January 2009.

[54] C R Phillips and M M Fejer. Efficiency and phase of optical parametric amplification in chirped quasi-phase-matched gratings. *Optics letters*, 35(18):3093–3095, 2010.

[55] C R Phillips, J S Pelc, and M M Fejer. Parametric processes in quasi-phasematching gratings with random duty cycle errors. *Journal of the Optical Society of America B*, 30(4):982–993, 2013.

[56] Ziya Gurkan Figen and Onur Akin. Red beam generation based on aperiodically poled lithium niobate. *Optics Communications*, 317:67–77, April 2014.

[57] Huw E Major, Corin B E Gawith, and Peter G R Smith. Gouy phase compensation in quasi phase matching. (i):1–5, 2007.

[58] P Honzatko, P Peterka, and J Kanka. Modulational-instability sigma-resonator fiber laser. *Optics letters*, 26(11):810–2, 2001.

[59] Thomas J. Kane and Robert L. Byer. Monolithic, unidirectional single-mode Nd:YAG ring laser. *Optics Letters*, 10(2):65, February 1985.

[60] Svyatoslav Kharitonov and Camille-Sophie Bres. Isolator-free unidirectional thulium-doped fiber laser. *Light: Science & Applications*, 4(10):e340, 2015.

[61] R Paschotta. Ring lasers. https://www.rp-photonics.com/ring-lasers.html. Accessed: 2017-11-10.

[62] Feifei Yin, Sigang Yang, Hongwei Chen, Minghua Chen, and Shizhong Xie. Tunable single-longitudinal-mode Ytterbium all fiber laser with saturable-absorber-based auto-tracking filter. *Optics Communications*, 285(10-11):2702–2706, 2012.

[63] R. Paschotta, D. J. B. Brinck, S. G. Farwell, and D. C. Hanna. Resonant loop mirror with narrow-band reflections and its application in single-frequency fiber lasers. *Applied Optics*, 36(3):593, January 1997.

[64] Orazio Svelto. *Principles of Lasers*. Springer US, Boston, MA, 2010.

[65] Namkyoo Park, Jay W. Dawson, Kerry J. Vahala, and Calvin Miller. All fiber, low threshold, widely tunable single-frequency, erbium-doped fiber ring laser with a tandem fiber Fabry-Perot filter. *Applied Physics Letters*, 1991.

[66] A. Gloag, N. Langford, K. McCallion, and W. Johnstone. Continuously tunable single-frequency erbium ring fiber laser. *Journal of the Optical Society of America B*, 13(5):921, 1996.

[67] Gautam Das and Zachary J. Chaboyer. Single-wavelength fiber laser with 250 mW output power at 1.57 um. *Optics Express*, 17(10):7750, 2009.

[68] Jay W. Dawson, Michael J. Messerly, Raymond J. Beach, Miroslav Y. Shverdin, Eddy A. Stappaerts, Arun K. Sridharan, Paul H. Pax, John E. Heebner, Craig W. Siders, and C.P.J. Barty. Analysis of the scalability of diffraction-limited fiber lasers and amplifiers to high average power. *Optics Express*, 16(17):13240, August 2008.

[69] C. J. Van Der Poel, J. D. Bierlein, J. B. Brown, and S. Colak. Efficient type I blue second-harmonic generation in periodically segmented KTiOPO4waveguides. *Applied Physics Letters*, 1990.

[70] Mool C. Gupta, W. P. Risk, Alan C.G. Nutt, and S. D. Lau. Domain inversion in KTiOPO4using electron beam scanning. *Applied Physics Letters*, 63(9):1167–1169, 1993.

[71] W P Risk. Periodic poling of KTiOPO/sub 4/ using an applied electric field - Electronics Letters. 30(18):1516–1517, 1994.

[72] G. Rosenman, A. Skliar, D. Eger, M. Oron, and M. Katz. Low temperature periodic electrical poling of flux-grown KTiOPO4 and isomorphic crystals. *Applied Physics Letters*, 73(25):3650–3652, 1998.

[73] Thorlabs.com - Tutorials.

[74] Håkan Karlsson. *Fabrication of periodically poled crystals from the KTP family and their applications in nonlinear optics*. PhD thesis, 1999.

[75] H. Karlsson, F. Laurell, and L. K. Cheng. Periodic poling of RbTiOPO4 for quasi-phase matched blue light generation. *Applied Physics Letters*, 74(11):1519–1521, 1999.

[76] Carlota Canalias. *Domain Engineering in KTiOPO4*. PhD thesis, 2005.

[77] J. Wittborn, C. Canalias, K. V. Rao, R. Clemens, H. Karlsson, and F. Laurell. Nanoscale imaging of domains and domain walls in periodically poled ferroelectrics using atomic force microscopy. *Applied Physics Letters*, 80(9):1622–1624, 2002.

[78] Piezoresponse force microscopy. http://www.ncbi.nlm.nih.gov/pubmed/20823500. Accessed: 2017-10-22.

[79] Hoda Kianirad, Andrius Zukauskas, Thomas Frisk, Carlota Canalias, and Fredrik Laurell. Contact poling of Rb:KTiOPO4 using a micro-structured silicon electrode. *Optics Express*, 23(2):636–641, 2015.

[80] G M Gibson, G A Turnbull, M Ebrahimzadeh, M H Dunn, H Karlsson, G Arvidsson, and F Laurell. Temperature-tuned difference-frequency mixing in periodically poled KTiOPO4. *Applied Physics B-Lasers and Optics*, 67(5):675–677, 1998.

[81] Ben Henderson, Amir Khodabakhsh, Markus Metsala, Irene Ventrillard, Florian M. Schmidt, Daniele Romanini, Grant A. D. Ritchie, Sacco te Lintel Hekkert, Raphael Briot, Terence Risby, Nandor Marczin, Frans J. M. Harren, and Simona M. Cristescu. Laser spectroscopy for breath analysis: towards clinical implementation. *Applied Physics B*, 124(8):161, August 2018.

[82] Laurent M. Paardekooper, Geert Van Den Bogaart, Matthijs Kox, Ilse Dingjan, Anne H. Neerincx, Maura B. Bendix, Martin Ter Beest, Frans J.M. Harren, Terence Risby, Peter Pickkers, Nandor Marczin, and Simona M. Cristescu. Ethylene, an early marker of systemic inflammation in humans. *Scientific Reports*, 7(1):2–11, 2017.

[83] J. S. Li, W. Chen, and H. Fischer. Quantum Cascade Laser Spectrometry Techniques: A New Trend in Atmospheric Chemistry. *Applied Spectroscopy Reviews*, 48(7):523–559, October 2013.

[84] Zhenhai Wang, Pengfei Fu, and Xing Chao. Laser Absorption Sensing Systems : Challenges, Modeling, and Design Optimization. *Applied Sciences*, 9(13):2723–2750, 2019.

[85] L. S. Rothman, I. E. Gordon, Y. Babikov, A. Barbe, D. Chris Benner, P. F. Bernath, M. Birk, L. Bizzocchi, V. Boudon, L. R. Brown, A. Campargue, K. Chance, E. A. Cohen, L. H. Coudert, V. M. Devi, B. J. Drouin, A. Fayt, J. M. Flaud, R. R. Gamache, J. J. Harrison, J. M. Hartmann, C. Hill, J. T. Hodges, D. Jacquemart, A. Jolly, J. Lamouroux, R. J. Le Roy, G. Li, D. A. Long, O. M. Lyulin, C. J. Mackie, S. T. Massie, S. Mikhailenko, H. S.P. Müller, O. V. Naumenko, A. V. Nikitin, J. Orphal, V. Perevalov, A. Perrin, E. R. Polovtseva, C. Richard, M. A.H. Smith, E. Starikova, K. Sung, S. Tashkun, J. Tennyson, G. C. Toon, Vl G. Tyuterev, and G. Wagner. The HITRAN2012 molecular spectroscopic database. *Journal of Quantitative Spectroscopy and Radiative Transfer*, 130:4–50, November 2013.

[86] Roie Knaanie, Jiri Sebek, Masashi Tsuge, Nanna Myllys, Leonid Khriachtchev, Markku Rasanen, Brian Albee, Eric O. Potma, and R. Benny Gerber. Infrared Spectrum of Toluene: Comparison of Anharmonic

Isolated-Molecule Calculations and Experiments in Liquid Phase and in a Ne Matrix. *Journal of Physical Chemistry A*, 120(19):3380–3389, 2016.

[87] I.E. Gordon, L.S. Rothman, C. Hill, R.V. Kochanov, Y. Tan, P.F. Bernath, M. Birk, V. Boudon, A. Campargue, K.V. Chance, B.J. Drouin, J.-M. Flaud, R.R. Gamache, J.T. Hodges, D. Jacquemart, V.I. Perevalov, A. Perrin, K.P. Shine, M.-A.H. Smith, J. Tennyson, G.C. Toon, H. Tran, V.G. Tyuterev, A. Barbe, A.G. Csaszar, V.M. Devi, T. Furtenbacher, J.J. Harrison, J.-M. Hartmann, A. Jolly, T.J. Johnson, T. Karman, I. Kleiner, A.A. Kyuberis, J. Loos, O.M. Lyulin, S.T. Massie, S.N. Mikhailenko, N. Moazzen-Ahmadi, H.S.P. Muller, O.V. Naumenko, A.V. Nikitin, O.L. Polyansky, M. Rey, M. Rotger, S.W. Sharpe, K. Sung, E. Starikova, S.A. Tashkun, J. Vander Auwera, G. Wagner, J. Wilzewski, P. Wcislo, S. Yu, and E.J. Zak. The hitran2016 molecular spectroscopic database. *Journal of Quantitative Spectroscopy and Radiative Transfer*, 2017.

[88] Wikipedia contributors. Toluene — Wikipedia, the free encyclopedia, 2019. [Online; accessed 18-December-2019].

[89] Pawel Kluczynski, Jörgen Gustafsson, Åsa M. Lindberg, and Ove Axner. Wavelength modulation absorption spectrometry - an extensive scrutiny of the generation of signals. *Spectrochimica Acta Part B: Atomic Spectroscopy*, 56(8):1277–1354, August 2001.

[90] Simona M. Cristescu, Julien Mandon, Denis Arslanov, Jérôme De Pessemier, Christian Hermans, and Frans J.M. Harren. Current methods for detecting ethylene in plants. *Annals of Botany*, 111(3):347–360, 2013.

[91] Fred B. Abeles and Howard E. Heggestad. Ethylene: An Urban Air Pollutant. *Journal of the Air Pollution Control Association*, 23(6):517–521, 1973.

[92] Wikipedia contributors. Ethylene — Wikipedia, the free encyclopedia, 2019. [Online; accessed 15-January-2020].

[93] Principles of lock-in detection. https://www.zhinst.com/others/resources/principles-of-lock-in-detection. Accessed: 2018-12-14.

[94] Michal Nikodem, Damien Weidmann, Clinton Smith, and Gerard Wysocki. Signal-to-noise ratio in chirped laser dispersion spectroscopy. *Optics Express*, 20(1):644, 2012.

List of author's publications related to the PhD thesis

[P1] **Yauhen Baravets**, Pavel Honzatko, Filip Todorov, and Petar Gladkov. Narrowband widely tunable cw mid-infrared generator based on difference frequency generation in periodically poled ktp and kta crystals. *Optical and Quantum Electronics*, 48(5):286, may 2016.

[P2] Pavel Honzatko, **Yauhen Baravets**, and Ashwin Kumar Myakalwar. Single-frequency fiber laser based on a fiber ring resonator filter tunable in a broad range from 1023 nm to 1107 nm. *Opt. Lett.*, 43(6):1339–1342, Mar 2018.

[P3] **Y. Baravets**, P. Dvorak, F. Todorov, J. Ctyroky, P. Peterka, and P. Honzatko. Broadly tunable laser based on novel metallic resonant leaky- mode diffraction grating. *Opt. Express*, 28(3):4340–4346, Feb 2020.

Related conference talks and proceedings

[C1] **Y. Baravets**, P. Honzatko, and F. Todorov. Narrow band CW MIR generator based on the difference frequency generation in KTP crystal, February 2014. Presented at the *2nd Annual Conference of COST Action MP1204 and International Conference on Semiconductor Mid - IR Materials and Optics SMMO2014*, Philipps University, Marburg, Germany.

[C2] **Y. Baravets**, Petr Dvorak, Filip Todorov, Jiri Ctyroky, Pavel Peterka, and Pavel Honzatko. Broadly tunable laser based on novel leaky-waveguide metallic diffraction grating. In *Laser Congress 2019 (ASSL, LAC, LS&C)*, page AM3A.3. Optical Society of America, 2019.

[C3] **Yauhen Baravets**, Filip Todorov, and Pavel Honzatko. High-power thulium-doped fiber laser in an all-fiber configuration. In 20th Slovak-Czech-Polish Optical Conference on Wave and Quantum Aspects of Contemporary Optics, volume 10142 of *Proceedings of SPIE*, page 101420G. International Society for Optics and Photonics, 2016.

[C4] **Yauhen Baravets**, Pavel Honzátko, and Filip Todorov. Dvoumikronové vysokovýkonové thuliem dopované vláknové lasery a jejich aplikace. In *Optické komunikace 2016*, Praha, ČR, 2016.

[C5] **Yauhen Baravets**, Pavel Honzátko, Filip Todorov, and Ondřej Moravec. Panoramatická laserová absorpční spektroskopie. In *Laser 56*, Třešť, ČR, 2016.

[C6] **Yauhen Baravets**, Ashwin Kumar Myakalwar, and Pavel Honzatko. Phase noise measurements of single-frequency widely tunable ytterbium fiber laser. In *The 8th International Conference on Photonics, Devices and Systems*, Photonics Prague 2017, 2017.

[C7] **Y. Baravets**, P. Honzatko, and P. Koska. Efficiency enhancement of the MIR DFG laser source based on periodically poled KTP crystal by optimal focusing conditions. In *The 8th International Conference on Photonics, Devices and Systems,* Photonics Prague 2017, 2017.

[C8] Pavel Honzatko, **Yauhen Baravets**, Shyamal Mondal, Pavel Peterka, and Filip Todorov. Coherent sources for mid-infrared laser spectroscopy. In 20th Slovak-czech-polish optical conference on wave and quantum aspects of contemporary optics, volume 10142 of *Proceedings of SPIE*, page 1014202. International Society for Optics and Photonics, 2016.

[C9] **Y. Baravets**, P. Honzatko, F. Todorov, and P. Gladkov. Comparison of tunable narrow-band CW mid-IR generators based on the difference frequency generation in KTP and KTA crystals, 2015. Presented at *COST MP1204 Conference & SMMO 2015 Conference* Prague, April 9, 2015.

[C10] P. Honzatko, **Y. Baravets**, F. Todorov, and P. Gladkov. Comparison of widely tunable narrow-band CW MIR generators based on the difference frequency generation in KTP and KTA crystals. In *Advanced Solid State Lasers*, page ATh2A.36, Washington, D.C., 2014. OSA.

[C11] P. Honzatko, **Y. Baravets**, F. Todorov, and P. Gladkov. Tunable narrow- band CW MIR generator based on the difference frequency generation in KTP crystal, 2014. Paper presented at *MIOMD 2014*, Montpellier, France.

Other publications and conference talks of the author

[O1] Jan Aubrecht, Jakub Cajzl, Pavel Peterka, Pavel Honzatko, Pavel Koska, **Yauhen Baravets**, Martin Becker, Ondrej Podrazky, Filip Todorov, and Ivan Kasik. Characterization of double-clad thulium-doped fiber with increased quantum conversion efficiency. In Microstructured and Specialty Optical Fibres IV, volume 9507 of *Proceedings of SPIE*, page 95070P, may 2015.

[O2] Pavel Koska, **Yauhen Baravets**, Pavel Peterka, Jan Bohata, and Michael Pisarik. Mode-field adapter for tapered-fiber-bundle signal and pump combiners. *Applied Optics*, 54(4):751, feb 2015.

[O3] M. Pisarik, P. Peterka, S. Zvanovec, **Y. Baravets**, F. Todorov, I. Kasik, and P Honzatko. Fused fiber components for "eye-safe" spectral region around 2μm. *Optical and Quantum Electronics*, 46(4):603–611, 2014.

[O4] Pavel Honzatko, **Yauhen Baravets**, Ivan Kasik, and Ondrej Podrazky. Wideband thulium-holmium-doped fiber source with combined forward and backward amplified spontaneous emission at 1600–2300 nm spectral band. *Optics Letters*, 39(12):3650, jun 2014.

[O5] P. Koska, P. Peterka, P. Honzatko, O. Podrazky, J. Aubrecht, F. Todorov, **Y. Baravets**, and I. Kasik. Pump Absorption Enhancement In Double-Clad Fiber Lasers By Coiling And Twisting, September 2016. Presented at the *20th Slovak-Czech-Polish Optical Conference on Wave and Quantum Aspects of Contemporary Optics*, Jasna, Slovakia.

[O6] J. Aubrecht, P. Peterka, I. Kasik, O. Podrazky, J. Cajzl, A. Benda, **Y. Baravets**, and P. Honzatko. Characterization And Numerical Modeling Of Holmium-Doped Fibers With Various Concentrations For Fiber Lasers, September 2016. Presented at the *20th Slovak-Czech-Polish Optical Conference on Wave and Quantum Aspects of Contemporary Optics*, Jasna, Slovakia.

[O7] **Yauhen Baravets**, Pavel Honzatko, Filip Todorov, Pavel Peterka, Ivan Kasik, Pavel Koska, and Ondrej Podrazky. 60W CW thuliovy vlaknovy laser pro prumyslove a medicinske aplikace, October 2015. Presented at *Multioborova konference LASER 55*, Trest.

[O8] **Yauhen Baravets**, Pavel Honzatko, and Filip Todorov. Dvoumikronove vysokovykonove thuliem dopovane vlaknove lasery a jejich aplikace, November 2017. Presented at *Opticke komunikace 2016*, Praha, CR.

[O9] Pavel Honzatko and **Yauhen Baravets**. Vyzkum optickych vlaken, vlaknovych laseru, zesilovacu a jejich aplikaci, November 2017. Presented at *Opticke komunikace 2016*, Praha, CR.

[O10] F. Todorov, **Y. Baravets**, P. Honzatko, P. Peterka, P. Koska, I. Kasik, and O. Podrazky. 60W Thulium Fiber Laser for Industrial and Medical Applications, Aipril 2016. Presented at *COST MP1401* Annual Conference, Zadar, Croatia.

[O11] Martin Vanek, Jan Vanis, **Yauhen Baravets**, Filip Todorov, Jiri Ctyroky, and Pavel Honzatko. Fiber facet gratings for high power fiber lasers. In Karel Fliegel and Petr Pata, editors, Photonics, Devices, and Systems VII, volume 10603 of *Proceedings of SPIE*, pages 114–119. International Society for Optics and Photonics, SPIE, 2017.

[O12] M. Vanek, J. Vanis, **Y. Baravets**, F. Todorov, J. Ctyroky, and P. Honzatko. Thulium-doped high-power fiber laser with a polarizing diffraction grating on the fiber facet, March 2017. Presented at *COST MP1401*, Tel Aviv, Israel.

[O13] Martin Vanek, Jan Vanis, **Yauhen Baravets**, Filip Todorov, Jiri Ctyroky, and Pavel Honzatko. Fiber facet gratings for use in high-power fiber lasers, October 2017. Presented at the *5th Workshop on Specialty Optical Fiber and Their Applications (WSOF'2017)*, Limassol, Cyprus.

[O14] V. Puchy, F. Kovac, L. Falat, I. Petryshynets, R. Dzunda, M. Fides, M. Podobova, J. Mrazek, **Y. Baravets**, P. Honzatko, and S. Vytykacova. The effects of CO2 laser and thulium-doped fibre laser scribing on magnetic domains structure, coercivity, and nanohardness of Fe-3.2Si grain-oriented electrical steel sheets. *Kovove Materialy*, 56(6):389–395, 2018.

[O15] Pavel Koska, Pavel Peterka, Jan Aubrecht, Ondrej Podrazk, Filip Todorov, **Yauhen Baravets**, Pavel Honzatko, and Ivan Kasik. Enhanced Pump Absorption Efficiency in Coiled and Twisted Double-Clad Thulium-Doped Fibers. In *Advanced Solid State Lasers*, page ATu2A.23. OSA, 2015.

[O16] Martin Vanek, Jan Vanis, **Yauhen Baravets**, Filip Todorov, Jiri Ctyroky, and Pavel Honzatko. High-power fiber laser with a polarizing diffraction grating milled on the facet of an optical fiber. *Optics Express*, 24(26):30225, 2016.

[O17] Martin Vanek, Jan Vanis, **Yauhen Baravets**, Filip Todorov, Jiri Ctyroky, and Pavel Honzatko. Anti-reflection and polarizing photonic structures for high-power fiber applications. In Kyriacos Kalli, Jiri Kanka, Alexis Mendez, and Pavel Peterka, editors, *Proceedings of SPIE - The International Society for Optical Engineering*, volume 10232, page 102320W, may 2017.

[O18] Jan Aubrecht, Pavel Peterka, Pavel Honzatko, **Yauhen Baravets**, Michal Jelinek, Vaclav Kubecek, Maria Pawliszewska, Jaroslaw Sotor, Grzegorz Sobon, K.M. Krzysztof M. Abramski, and Ivan Kasik. Characterization of holmium fibers with various concentrations for fiber laser applications around 2.1 μm. In Micro-Structured And Specialty Optical Fibres IV, volume 9886 of *Proceedings of SPIE*, page 988607, apr 2016.

[O19] Pavel Koska, Pavel Peterka, Jan Aubrecht, Ondrej Podrazky, Filip Todorov, Martin Becker, **Yauhen Baravets**, Pavel Honzatko, and Ivan Kasik. Enhanced pump absorption efficiency in coiled and twisted double-clad thulium-doped fibers. *Optics Express*, 24(1):102, jan 2016.

[O20] P. Koska, **Y. Baravets**, P. Peterka, M. Pisarik, and J. Bohata. Optimized mode-field adapter for low-loss fused fiber bundle signal and pump combiners. In *Proceedings of SPIE - The International Society for Optical Engineering*, volume 9344, 2015.

[O21] **Y. Baravets**, P. Honzatko, F. Todorov, and P. Gladkov. Generation of mid-infrared radiation in nonlinear crystals using fiber lasers. *Fine Mechanics And Optics*, 5-6(5-6), 2015.